Title

Ultrafine V2O5-anchored 3D N-doped carbon nanocomposite with augmented dual-enzyme mimetic activity for evaluating total antioxidant capacity

Authors

Wang, Qi
Ding, Yongli
Dahlgren, Randy A
et al.

Publication Date

2023-04-01

DOI

10.1016/j.aca.2023.341072

Peer reviewed

Analytica Chimica Acta 1252 (2023) 341072

Contents lists available at ScienceDirect

Analytica Chimica Acta

journal homepage: www.elsevier.com/locate/aca

Ultrafine V_2O_5-anchored 3D N-doped carbon nanocomposite with augmented dual-enzyme mimetic activity for evaluating total antioxidant capacity

Qi Wang [a], Yongli Ding [a], Randy A. Dahlgren [b], Yue Sun [a], Jingjing Gu [a], Yuhao Li [a], Tingting Liu [a,c,**], Xuedong Wang [a,*]

[a] School of Environmental Science and Engineering, Suzhou University of Science and Technology, Suzhou, 215009, China
[b] Department of Land, Air and Water Resources, University of California, Davis, UC, 95616, USA
[c] Jiangsu Key Laboratory of Environmental Science and Engineering, Suzhou University of Science and Technology, Suzhou, 215009, China

HIGHLIGHTS

- A 3D-V_2O_5/NC nanocomposite is fabricated by a self-templating strategy.
- 3D-V_2O_5/NC has dual enzyme-mimetic activity (oxidase-like and catalase-like).
- Synergistic effect between N-doped carbon lamellae and multivalent V_2O_5 nanoparticles.
- This method provides a low detection limit and suitable recovery for TAC.
- Developed a smartphone-based colorimetric application (APP).

GRAPHICAL ABSTRACT

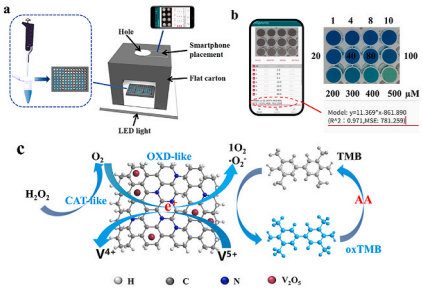

ARTICLE INFO

Handling Editor: Professor Chuck Henry

Keywords:
Vanadium pentoxide
3D-V_2O_5/NC nanocomposite
Dual-enzyme mimetic activity
Smartphone-based colorimetric sensor
Total antioxidant capacity
Superoxide anion

ABSTRACT

Total antioxidant capacity (TAC) can be evaluated by detecting the content of antioxidants, such as ascorbic acid, based on the enzyme-mimetic activity of nanomaterials. Herein, we fabricated a 3D-V_2O_5/NC nanocomposite using a self-templating strategy, which achieved ultrafine particles (~2.5 nm), a porous carbon layer, large specific surface area (152.4 m^2/g), N-doping and heterogeneous structure. The strong catalytic activity of 3D-V_2O_5/NC resulted from the integrated effect between the ultrafine structure of V_2O_5 nanoparticles and the 3D porous nitrogen-doped carbon framework, effectively increasing the number of active sites. This nanozyme presented a higher catalytic activity than its components or precursors in the nanocomposite (e.g., VN/NC, NC, V_2O_5, and VO_2/g-C_3N_4). ROS scavenging experiments confirmed that the dual enzyme-like activity of 3D-V_2O_5/NC (catalase-like and oxidase-like) resulted from their co-participation of $\cdot O_2^-$, h^+ and ·OH, among which $\cdot O_2^-$ played a crucial role in the catalytic color reaction. By virtue of the 3D-V_2O_5/NC nanoenzyme activity and TMB as a chromogenic substrate, the mixed system of 3D-V_2O_5/NC + TMB + H_2O_2 provided a low detection limit (0.03 μM) and suitable recovery (93.0–109.5%) for AA. Additionally, a smartphone-based colorimetric application was developed employing "Thing Identify" software to evaluate TAC in beverages. The colorimetric sensor and smartphone-detection platform provide a better or comparable analytical performance for TAC assessment in

* Corresponding author.
** Corresponding author. School of Environmental Science and Engineering, Suzhou University of Science and Technology, Suzhou, 215009, China.
E-mail addresses: liutt@mail.usts.edu.cn (T. Liu), zjuwxd@163.com (X. Wang).

https://doi.org/10.1016/j.aca.2023.341072
Received 6 January 2023; Received in revised form 7 March 2023; Accepted 7 March 2023
Available online 8 March 2023

comparison to commercial ABTS test kits. The newly developed smartphone-based colorimetric platform presents several prominent advantageous, such as low cost, simple/rapid operation, and feasibility for outdoor use.

1. Introduction

Owing to high catalytic efficiency, convenient large-scale preparation, and easy long-term storage, nanozymes are widely employed in biological and chemical sensing platforms [1,2]. Single enzyme activity of nanomaterials has been widely reported, especially for peroxidase (POD)-like activity [3,4]. In recent years, nanomaterials with multi-enzyme activities elicited great interest as they participate in multi-step/tandem reactions, where each enzyme is responsible for a single reaction step, thereby realizing the simultaneous assay of multiple chemicals. Moreover, the synergistic effects of multi-enzyme catalysts improve the catalytic efficiency of a single enzyme. For example, $Co_2V_2O_7$ possesses oxidase (OXD)-, POD-, and catalase (CAT)-like activities [5], 2D $MoSe_2$@PVP nanosheets have CAT, POD, superoxide dismutase (SOD), and glutathione peroxidase (GPx)-like activities [6], and NSC/$Co_{1-x}S$ has OXD and POD-like activities [7]. Notably, the underlying mechanisms regarding multi-enzyme activities of nanomaterials remain unclear as compared to single enzyme activity. However, it is clear from the literature that development of new nanozymatic materials with multi-enzyme activities holds great potential for analytical applications given their superior catalytic performance.

The strong catalytic activities of various vanadium-based hybrid materials (VO_x) have recently been demonstrated making them an excellent candidate for several practical applications. Due to its multiple oxidation states (V^{2+}, V^{3+}, V^{4+}, V^{5+}), VO_x easily forms nanocomposites with multivalence properties, which facilitates the construction of defect sites and the rapid transfer of electrons within nanomaterials. Consequently, these superior characteristics of VO_x offer great potential for use in procedures involving catalytic color development. For example, André and colleagues demonstrated that V_2O_5 nanowires had POD-like activity related to surface properties of the (010) lattice surface [8]. Further, Zeb and coworkers synthesized VO_x nanosheets containing a mixture of oxidation states, structures and phases using a simple "one-pot" method [9]. V_2O_5 nanoribbons have dual enzyme-mimetic activities (e.g., glucose oxidase-like (GOx) activity and POD-like activity) and can be used as a tandem nanoenzyme to construct an online optical detection platform for glucose assay [10]. Thus, VO_x has strong attributes for use as a highly stable and catalytic activity-regulated nanoenzyme for colorimetric analysis in biosensing due to their unique structural properties.

The synergistic effect among the components of composite nanomaterials can effectively enhance their enzyme-like activities. Layered porous carbon materials are beneficial in increasing exposure of active sites and promoting electron transfer [11]. The combination of porous carbon materials with metal oxide nanoparticles can increase the specific surface area of nanocomposites, while also serving as a diffusion substrate to prevent their agglomeration [12]. Among carbon materials, N-doped nanomaterials have several prominent advantages, such as high electrical conductivity, large specific surface area, and ease of functionalized modification. As a result, N-doped nanomaterials are widely used in the fields of energy storage, catalysis and chemical analysis. Hou and coworkers designed N-doped porous carbon with active magnesium sites (Mg/NC), which increased OXD-like activity by 10.9-fold compared to N-doped carbon (NC) [13]. Similarly, Lu's group synthesized Cu–N co-doped carbon (Cu-NC) nanosheets with highly exposed Cu-Nx sites, which increased POD-like activity of Cu-NC-700 by 15–19-fold as compared to Cu-doped carbon (Cu–C) and N-doped carbon (N–C) [14]. Liang et al. generalized some reports of composite carbon nanomaterials based on metal oxides or metal sulfides, and found that they all had highly enzyme-mimetic catalytic activities and superior physico-chemical properties [15]. Thus, the integration of carbon materials with hierarchical porous structure and metal oxides can be an effective strategy to improve the catalytic performance of nanoenzymes.

Common nanozyme-based colorimetric methods have some limitations for widespread practical applications, such as dependence on a spectrophotometer, in-lab operational requirements, and inconvenience for outdoor use. With the development of digital communication techniques, many smartphone-based analytical platforms have gained widespread application and provide several advantages, such as an integrated sensor system, low cost, ease of use, and portability [16]. Zhu and colleagues developed a portable colorimetric sensor using a smartphone platform based on the novel nanoenzyme MnCo@C for rapid/sensitive detection of ascorbic acid (AA), 2,4-dichlorophenol and epinephrine [17]. Similarly, our group pioneered a colorimetric platform for glucose assay employing a high vacancy Fe_3S_4 nanozyme and "Thing identify" software deployed on a smartphone [18].

Informed by previous research developments, we herein prepared a 3D-V_2O_5/NC nanocomposite using a self-templating strategy in which V_2O_5 nanoparticles were dispersed and anchored onto N-doped carbon nanosheets (NCs). Based on the high catalytic activity of 3D-V_2O_5/NC and TMB as a chromogenic substrate, a colorimetric platform was developed for quantification of total antioxidant capacity (TAC). TAC represents the total antioxidants that regulate oxidative stress and ensure redox homeostasis in organisms. In this study, we used AA as a representative species of TAC. Further, a colorimetric sensing platform based on smartphone visualization was constructed using "Thing Identify" application (APP) software, which enables rapid field detection of trace TAC concentrations. The newly developed colorimetric method demonstrates great potential for conventional monitoring of TAC in complex pharmaceutical and food matrices.

2. Experimental section

2.1. Chemicals and materials

All chemicals used in this study were of analytical or chromatographic grade and purchased from Adams (Shanghai, China), including ascorbic acid (AA, 99.0%), hydrogen peroxide (H_2O_2, 30%), acetic acid (ACA, ≥98.0%), sodium acetate (CH_3COONa, 99.0%), ethanol (99.7%), dimethyl sulfoxide (DMSO, ≥99.0%), *p*-benzoquinone (PBQ, 99.2%), ethylene diamine tetraacetic acid (EDTA, 99.5%), sucrose (Suc, ≥99.0%), D-histidine (His, 99.5%), D-galactose (Gal, 99.5%), D-serine (Ser, 99.5%), L-tyrosine (Tyr, 99%), glycine (Gly, 99.0%), D(+)-tryptophan (Try, 99.0%), glucose (Glu, 99.0%), fructose (Fru, 99.0%), citric acid (CA, 98%), L(−)-malic acid (H_2Mi, 98.0%), L-cysteine (L-Cys, 98.0%), glutathione (GSH, 98.0%), uric acid (UA, 98.0%), 2,2′-azino-bis (3-ethylbenzothiazoline-6-sulfonic acid) (ABTS, 97.0%), and O-phenylenediamine (OPD, 99%). Ammonium metavanadate (NH_4VO_3) with purity ≥99.0% was obtained from Sigma-Aldrich (Shanghai, China) and isopropyl alcohol (IPA, ≥99.7%) and 3,3′,5,5′-tetramethylbenzidine (TMB) were procured from Aladdin (Shanghai, China). Anhydrous oxalic acid (OXA, 98.0%) and dicyandiamide (DCA, 99.0%) were obtained from Maclean (Shanghai, China). TAC assay kits using the ABTS method were procured from Beyotime Biochemical Technology (Shanghai, China). All reagents were used without further purification, and ultrapure water (>18.2 MΩ) was generated with a Milli-Q system (Bedford, MA, USA).

2.2. Analytical instruments

A model OTF-1200 tube furnace (Hefei, China) was used to calcine the required nanomaterials. Crystalline-phase identification was

assessed using X-ray diffraction (XRD) with Cu Kα radiation (D8 Advance, Bruker, Germany). Morphology of the synthesized nanocomposites was observed using a Zeiss Merlin Sigma 300 SEM (Carl Zeiss SMT AG, Germany), as well as a Talos F200X G2 TEM (TEM; FEI, USA). Fourier transform infrared (FT-IR) spectra were recorded on a Nicolet iN 10 instrument (Thermo Fisher Scientific, USA) using a KBr matrix. Brunauer-Emmett-Teller (BET) surface area was determined by N_2 adsorption at 77K using a Quadrasorb SI system (USA). Additional characterization of physicochemical properties for the synthesized nanomaterials included X-ray photoelectron spectroscopy (K-Alpha + type; Thermo Scientific, USA), thermal analysis by DSC/DTA-TG (STA449 F3; NETZSCH, Germany), microscopic laser Raman spectroscopy (Renishaw inVia, UK), and electron paramagnetic resonance/electron spin resonance (EPR/ESR) spectroscopy (EMXplus-6/1; Bruker, Germany).

2.3. Preparation of the 3D-V_2O_5/NC nanocomposite and intermediate products

2.3.1. Preparation of 3D-V_2O_5/NC nanocomposite

The 3D-V_2O_5/NC nanocomposite was synthesized using a self-templating strategy. Firstly, 0.42 g OXA and 0.23 g NH_4VO_3 were dissolved in 80 mL of deionized water to form a homogeneous solution. Then, 4.0 g of DCA was added and dried in an oil bath at 80 °C. The resulting precursors were calcined at 800 °C for 2 h in a N_2 atmosphere at a heating rate of 2 °C/min to obtain the VN/NC composites. Finally, the VN/NC was heated to 280 °C in an air atmosphere at a heating rate of 1 °C/min and held for 8 h to prepare the 3D-V_2O_5/NC nanocomposite.

2.3.2. Preparation of VO_2/g-C_3N_4

The operational procedures were similar as the synthesis of 3D-V_2O_5/NC, except that the precursors were heated in a N_2 atmosphere to 550 °C and held for 2 h.

2.3.3. Preparation of NC

Briefly, 0.1 g of glucose and 1.0 g of DCA were dissolved in deionized water. After stirring and drying in an oil bath at 80 °C, the resultant precursor was calcined in a N_2 atmosphere at 800 °C for 2 h at a heating rate of 2 °C/min.

2.4. Enzyme-like activity of 3D-V_2O_5/NC and its steady-state kinetics

By employing TMB as a chromogenic substrate, a series of colorimetric reactions were conducted to investigate the enzyme-mimetic activity of the 3D-V_2O_5/NC nanocomposite. After the reaction of 3D-V_2O_5/NC with H_2O_2, the absorbance intensity at 652 nm (A_{652}) was measured by a UV-5500PC spectrophotometer. Briefly, 60 μL of 250 μg/mL 3D-V_2O_5/NC suspension was added to 1700 μL of NaAc-HAc buffer solution (20 mM, pH = 3.6). Then, 200 μL of 6 mM TMB and 40 μL of 5 mM H_2O_2 were added sequentially to the above solution. The A_{652} values were determined after a 20-min incubation at 30 °C and filtration through a 0.45-μm cellulose membrane filter.

The steady-state kinetics of 3D-V_2O_5/NC were analyzed at 30 °C and a constant H_2O_2 level (5 mM) using a varying TMB concentration (0.01, 0.02, 0.03, 0.04, 0.05, 0.06, 0.07, 0.08, 0.09, and 1.0 mM). The catalytic kinetics were also investigated at a constant TMB level (6 mM) and varying H_2O_2 concentration (0.01, 0.03, 0.04, 0.06, 0.07, 0.08, 0.09, 0.1, 0.2, 0.4, 0.6, 0.8 mM). Catalytic parameters for the steady-state kinetics were determined by fitting the A_{652} data to the Michaelis-Menten equation (1), which presents the relationship between the conversion rate of a given substrate and the substrate concentration by an enzyme (in this case 3D-V_2O_5/NC):

$$1/V=(K_m/V_{max})(1/[S])+1/V_{max} \quad (1)$$

where *Km* is the Michaelis-Menten constant, V_{max} is the maximum reaction rate, and *[S]* is the TMB concentration.

2.5. Catalytic mechanisms associated with the enzyme-like activity of 3D-V_2O_5/NC

Previous studies have confirmed the scavenging capacity of IPA, EDTA, NaN_3 and PBQ for hydroxyl radicals (·OH), electron vacancies (h^+), singlet oxygen ($^1O_2$) and superoxide radicals ($\cdot O_2^-$), respectively [19,20]. To determine the type of ROS involved in the catalytic reaction, we added 200 μL of each scavenger and 100 μL of 3D-V_2O_5/NC nanocomposite to 1.7 mL of H_2O_2-TMB solution and measured the A_{652} values after a 20-min incubation. According to changes in *Km* values, the predominant ROS promoting the catalytic reaction in the 3D-V_2O_5/N-C-H_2O_2-TMB system was identified.

The generation of ·OH, h^+, $^1O_2$, and $\cdot O_2^-$ was determined by EPR spectroscopy using DMPO spin-trapping adducts (DMPO: 5,5′-dimethyl-1-pyrroline N-oxide). ·OH, h^+, and $^1O_2$ were detected under the conditions of NaAc buffer (0.2 M, pH = 3.6) as a solvent and the concentration of 3D-V_2O_5/NC at 1 mg/mL. After holding light for 5 min at room temperature, the solution was sucked into a quartz capillary for EPR analysis. The detection of $\cdot O_2^-$ was carried out using methanol as a solvent, and the other operations were similar as the detection of ·OH, h^+, and $^1O_2$.

2.6. Construction of a colorimetric sensing platform based on the 3D-V_2O_5/NC

2.6.1. Colorimetric analysis of H_2O_2

A total volume of 2 mL NaAc-HAc buffer (pH 3.6, 200 mM), containing H_2O_2 (0–5 mM), 0.25 mg/mL 3D-V_2O_5/NC and 6 mM TMB, was incubated at 30 °C for 20 min. After transferring the resultant solution into a cuvette, the A_{652} value was determined by UV–vis spectroscopy, and the corresponding calibration plot was constructed between A_{652} and H_2O_2 concentration.

2.6.2. Colorimetric analysis of AA

As described above, a total volume of 2 mL NaAc-HAc buffer (pH 3.6, 200 mM) containing 5 mM H_2O_2, 0.25 mg/mL 3D-V_2O_5/NC, 6 mM TMB, and varying concentrations of AA (0.1–500 μM) was incubated at 30 °C for 20 min. Other operational conditions were held similar to the colorimetric analysis for H_2O_2.

To investigate the selectivity of the 3D-V_2O_5/NC/TMB/H_2O_2 system toward AA detection, a range of interfering substances were added, including metal ions (Na^+, K^+, Ca^{2+}, Mg^{2+}), amino acids (His, Ser, Gly, Try, L-Cys, and Tyr), saccharide (Fru, Suc and Gal), GSH, and UA. Also, Glu, CA, and H_2Mi commonly present in beverage ingredients were selected as interfering substances. The concentrations of AA, L-Cys, GSH, and UA were set at 1.0 mM, whereas metal ions and biological molecules were set at 10.0 mM.

To determine the reproducibility of the constructed colorimetric sensor for AA assay, the post-reaction solution was centrifuged at 5000 rpm for 3 min. The filtered 3D-V_2O_5/NC nanocomposites were washed and dried for colorimetric assay as described above, and the corresponding A_{652} values were determined to assess changes in absorbance intensity during reuse cycles.

2.7. AA assay for vitamin C tablets and TAC assessment for real-world beverage

To further verify the reliability and accuracy of this proposed method, we determined the contents of AA in various Vitamin C tablets, which were purchased from a local drugstore using TMB assay method. Vitamin C tablets were ground into powder and diluted by 20–40-fold with ultrapure water to ensure that the AA concentrations fell within the linear range of the calibration curve.

Using AA as a representative antioxidant, TAC was defined as molar

equivalent per liter of AA (AA mM/L). TAC tests were performed in six beverages procured from a local supermarket in Suzhou, China. Beverage samples were filtered through a 0.22-μm membrane filter and further diluted by 20–30-fold with ultrapure water. For the TAC assessment, 5 mM of H_2O_2, 0.25 mg/mL of 3D-V_2O_5/NC, 6 mM of TMB and 0.3 mL of the aforementioned diluted samples were added to 50 mL of 0.2 M NaAc-HAc buffer (pH 3.6). The mixed solution was incubated at 30 °C for 20 min, and then the A_{652} value was recorded and used for calculating molar equivalent of AA based on the linear equation of AA detection. Finally, TAC's evaluation was obtained by the absorbance conversion and multiplying by dilution fold. To perform recovery test, varying amounts of AA solution with a known concentration were fortified to the real samples and determined to obtain the value of equivalent AA.

2.8. Visual assessment of TAC using a smartphone-based platform

A practicable smartphone-based colorimetric sensor was developed as a low-cost and convenient assessment for TAC. The AA concentration was determined under optimized conditions in the mixed system of 3D-V_2O_5/NC + H_2O_2+TMB. A smartphone was used to capture chromaticity images, and the color intensity of the images were quantified using "Thing Identify" APP software, which was previously developed by our group [7,18]. The APP automatically recognized the images and converts them to RGB intensity values. Based on the relationship between color intensity and input concentration, a calibration curve is automatically established. Finally, the corresponding linear equation, correlation coefficient, and detected concentration are rapidly displayed on the screen. Fig. S1 provides detailed operational procedures for the smartphone-based TAC assessment.

3. Results and discussion

3.1. Synthesis and characterization of 3D-V_2O_5/NC

3.1.1. The synthesis of 3D-V_2O_5/NC

The mixed precursors of OXA, DCA, and NH_4VO_3 were first annealed at 550 °C under a N_2 atmosphere, during which DCA was converted to an intermediate graphitic carbon nitride (g-C_3N_4) and NH_4VO_3 was reduced to VO_2 [21] (See Scheme 1). The intermediates consist of crystals with varying nanometer sizes and a smooth surface with some agglomerated nanoparticles appearing on the surface to produce VO_2/g-C_3N_4 nanocomposites (Fig. S2a). After continuing the annealing at 800 °C in a N_2 atmosphere, a flake-like NC material was obtained with small nanoparticles uniformly dispersed on the NC surface (VN/NC, Fig. S2b) [22]. Finally, the resultant product was exposed to ambient air and calcined at 280 °C to acquire the final targeted nanocomposite (3D-V_2O_5/NC), which exhibited amorphous flakes coated with some fine particles (Fig. 1a and b). Process-wise, DCA was converted to g-C_3N_4 at ~530 °C and completely decomposed at a temperature above 700 °C [23]. Kuai and coworkers found that g-C_3N_4 was carbonized into the 3D mesoporous N-doped carbon network at 800 °C and formed VN with VO_2 due to the electrostatic interaction between the protonation of lone pair electrons of pyridinic N in g-C_3N_4 and $(VO)_2(C_2O_4)_3^{2-}$ pieces [24]. The 3D carbon network formed during the later pyrolysis protected the V_2O_5 from irreversible polymerization and aggregation, resulting in the formation of a porous composite with ultrafine nanoparticles.

3.1.2. The morphology of 3D-V_2O_5/NC

SEM images of NC showed a smooth and porous surface (Fig. S2c). After attaching NC to V_2O_5 nanomaterials, it was observed that some small particles adhered to the surface of the porous carbon layer, forming a heterogeneous structure (Fig. 1a). Further, SEM and TEM observations of V_2O_5 nanocrystals showed ultra-small average size of 2.5 nm that were uniformly immobilized on the porous carbon surface (Fig. 1a and b). HRTEM observation found different lattice layers with a spacing of 0.21 nm for the (211) crystal axis of V_2O_5 and 0.34 nm for the (002) crystal axis of carbon (Fig. 1c). The uniform distribution of C, N, V and O in the nanocomposites was clearly exhibited by EDS mapping (Fig. 1d), which further demonstrated the uniform dispersion of V_2O_5 nanoparticles. The mass percentages of C, N, V and O in the 3D-V_2O_5/NC were 21.8%, 4.9%, 43.1% and 30.2%, respectively (Fig. S3).

3.1.3. Specific surface area of 3D-V_2O_5/NC

The specific surface area of 3D-V_2O_5/NC was assessed via a series of N_2 adsorption/desorption analyses. A wide type-II isotherm with hysteresis lines and a pore distribution of 2–30 nm was observed in the 3D-V_2O_5/NC evidencing its mesoporous structure (Fig. S4). The BET surface area of 3D-V_2O_5/NC was 152.4 m^2/g, while those of NC, VO_2/g-C_3N_4, VN\NC and commercial V_2O_5 were 321.9 m^2/g, 53.1 m^2/g, 446.3 m^2/g and 7.9 m^2/g, respectively. By way of contrast, the BET surface area of 3D-V_2O_5/NC was larger than that of commercial V_2O_5, but lower than NC (Table S1). This was mainly due to the loading of smaller V_2O_5 nanoparticles on the surface and pore channels of the carbon material, thereby leading to a slight decrease in surface area. Notably, the porous structure and larger surface area of 3D-V_2O_5/NC increase its surface adsorption and active sites, which enhance the potential for reaction with target molecules and promote electron transfer, thus improving the enzyme-mimetic catalytic activity.

3.1.4. FT-IR analysis of 3D-V_2O_5/NC

The FT-IR spectrum of 3D-V_2O_5/NC was divided into three main regions: 450-1050 cm^{-1}, 1200-1650 cm^{-1} and 3100-3500 cm^{-1} (Fig. 1e). Peaks at 3100 and 3500 cm^{-1} are attributed to the stretching vibrations of N–H and O–H, respectively [25]. The absorption peaks located at ~565 cm^{-1} and 765 cm^{-1} belong to V–O–V stretching vibration, and 1015 cm^{-1} to the stretching vibration of V═O, highlighting the presence of V_2O_5 particles in the sample [26]. Additional peaks at

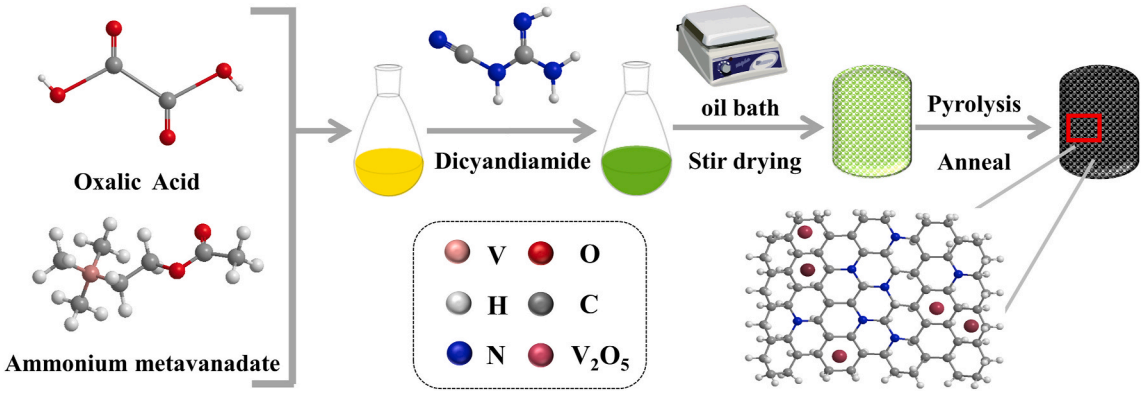

Scheme 1. Schematic for the synthesis of 3D-V_2O_5/NC nanocomposite.

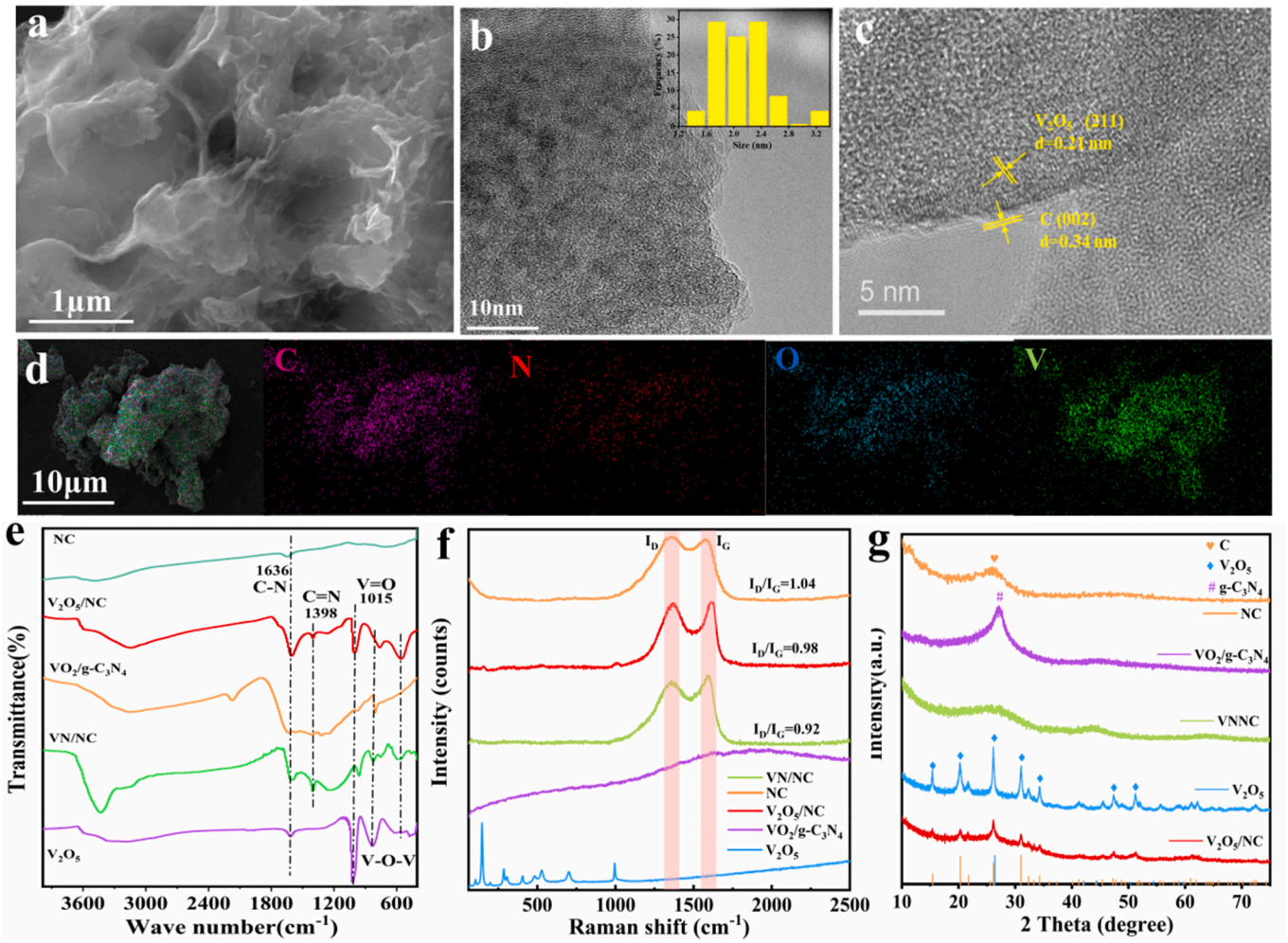

Fig. 1. (a) SEM image; (b) TEM image and size distribution (insert); (c) HRTEM image; (d) Elemental mapping; (e) FTIR spectra; (f) Raman spectra; and (g) XRD patterns of 3D-V_2O_5/NC.

1636 and 1398 cm^{-1} are attributable to the C–N and C═N stretching vibrations, respectively, providing compelling evidence for the presence of NC in the 3D-V_2O_5/NC nanocomposite [27].

3.1.5. Raman analysis of 3D-V_2O_5/NC

Raman spectroscopy identified two characteristic peaks at 1334 cm^{-1} (D band) and 1570 cm^{-1} (G band) in both NC and 3D-V_2O_5/NC (Fig. 1f). The D-band represents the disordered carbon or graphite structural defects, whereas the G-band is related to the graphitization level [28]. The peak intensity ratios of the D band to G band (I_D/I_G) were 1.04 and 0.98 for NC and 3D-V_2O_5/NC, respectively, documenting the presence of abundant defects in the porous carbon structure. Compared to NC, the slightly lower I_D/I_G value for 3D-V_2O_5/NC may be attributed to the pyrolysis process incorporating some V_2O_5 nanoparticles into defect sites, thereby reducing the disorder [29].

3.1.6. XRD analysis of 3D-V_2O_5/NC

XRD was used to evaluate the phase purity and crystallinity of the 3D-V_2O_5/NC nanocomposites (Fig. 1g). As for VO_2/g-C_3N_4, the peak at $2\theta = 26.1$ implies the formation of g-C_3N_4 during annealing [30], whereas the absence of a VO_2 signal may be ascribed to its amorphous structure at low annealing temperatures (≤550 °C). In contrast, the high crystallinity of 3D-V_2O_5/NC was apparent from the sharp peaks at 15.3, 20.3, 21.7, 26.1 and 31.0, belonging to the (200), (001), (101), (110) and (301) crystal planes, respectively, which matched with the standard card of vanadium pentoxide (PDF#41–1426). However, the peak intensities for 3D-V_2O_5/NC were significantly weaker compared to pure V_2O_5, which is attributed to the substantially reduced particle size, a common phenomenon with constructed nanomaterials having ultrafine particle sizes [31]. These diffraction data provide compelling evidence for the successful preparation of a 3D-V_2O_5/NC nanocomposite with a high purity level.

3.1.7. XPS analysis of 3D-V_2O_5/NC

The elemental composition and surface oxidation state of the 3D-V_2O_5/NC nanocomposite were assessed by XPS. The percentages of V, C, N and O in the nanocomposites were 19.3%, 47.4%, 4.6% and 28.7%, respectively, demonstrating the presence of N-doped carbon nanosheets of VO_x (Fig. S5). The two peaks at 516.8 eV and 524.0 eV denote V^{5+} (2p 3/2) and V^{5+} (2p 1/2), respectively (Fig. 2a), whereas the peak at 515.4 eV represents V^{4+} (2p 3/2). The presence of V^{4+} in the nanocomposite confirms that the reducing atmosphere (CO and NO) during calcination caused the reduction of some V^{5+} to V^{4+} [32]. As exhibited in Fig. 2b, the N1s spectra were deconvoluted into three peaks (398.7, 399.6, and 401 eV) attributable to pyridine-N, pyrrole-N and graphite-N, respectively [33]. N doping was conducive to improving electron transfer in the 3D-V_2O_5/NC nanocomposite, thereby greatly enhancing the catalytic performance. Pyridine-N and pyrrole-N in nitrogen-doped carbon-based nanomaterials have been well documented [34]. The deconvolution of the C1s spectrum produced three peaks at 284.1, 285.3 and 287.7 eV, corresponding to C–C, C═N–C and C–N, respectively (Fig. 2c). The formation of C═N–C and C–N further confirms the

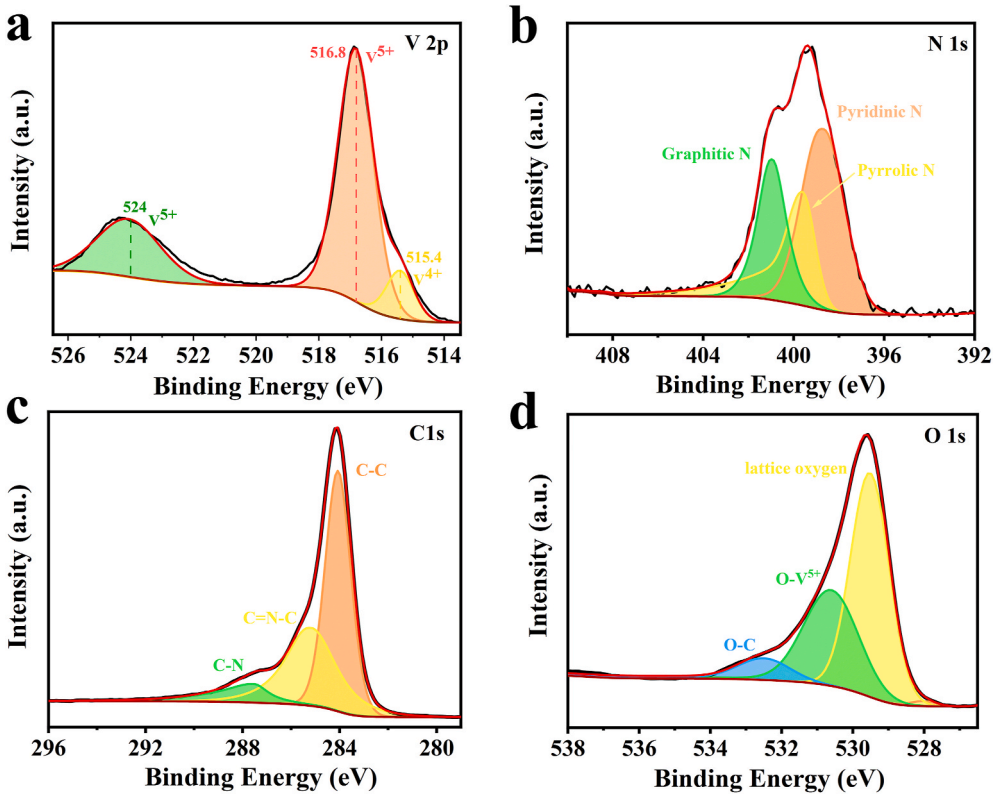

Fig. 2. High-resolution XPS spectra for 3D-V_2O_5/NC composite: (a) V 2p, (b) N 1s, (c) C 1s and (d) O 1s.

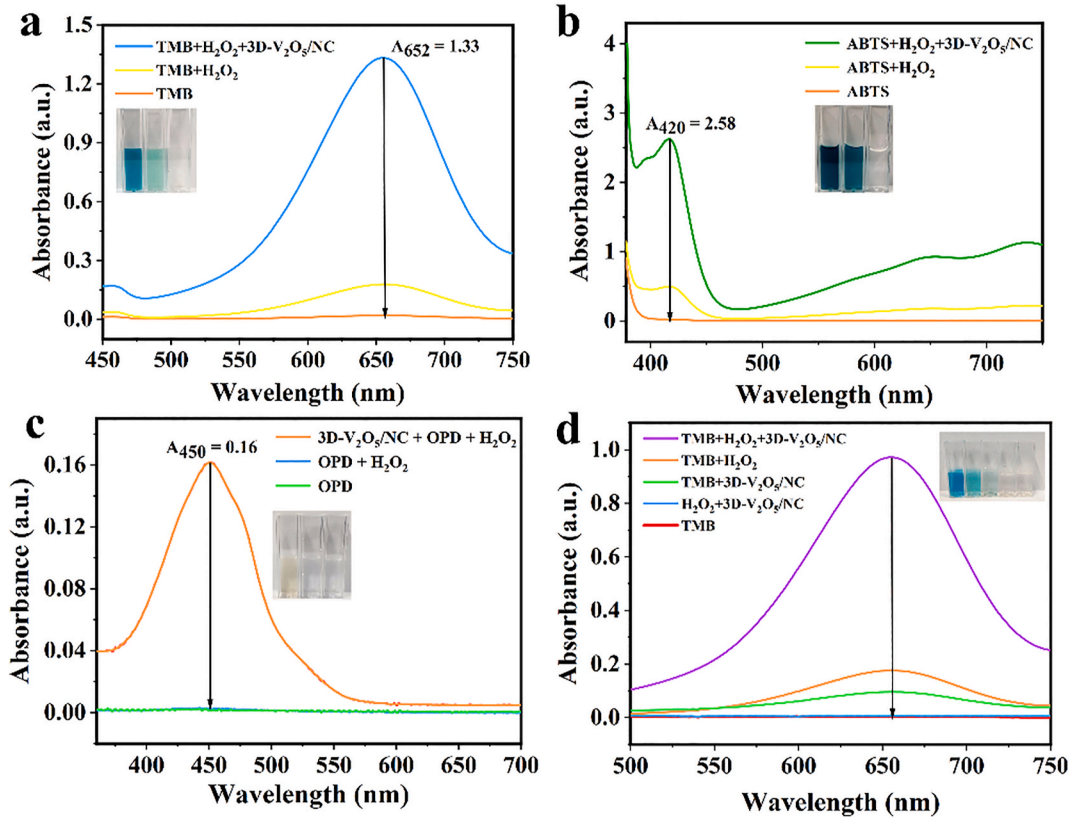

Fig. 3. UV–vis absorption spectra of TMB (a), ABTS (b) and OPD (c) catalyzed by 3D-V_2O_5/NC. (d) UV–vis absorption spectra and photographs of color changes in different reaction systems after a 20-min incubation. (For interpretation of the references to color in this figure legend, the reader is referred to the Web version of this article.)

successful doping of N atoms into the carbon-based materials. Further, the O1s spectrum was deconvoluted into two main peaks at 529.6 eV and 530.4 eV, which corresponded to lattice oxygen and O–V^{5+} functional groups in the 3D-V_2O_5/NC (Fig. 2d). The minor peak at 532.6 eV was attributable to C–O, and these observations highlighted the presence of V_2O_5 [35]. The overall results from SEM, XRD, EDS, XPS, Raman and FT-IR analyses provide compelling evidence that a 3D-V_2O_5/NC nanocomposite was successfully prepared.

3.2. Construction of a colorimetric sensing platform based on the 3D-V_2O_5/NC-TMB-H_2O_2 mixed system

3.2.1. Screening of the chromogenic substrates

To investigate the enzyme-like activity of the 3D-V_2O_5/NC nanocomposite, three common chromogenic substrates (TMB, ABTS and OPD) were assessed for their color development. The reaction system without a chromogenic substrate was used as a blank control. The reaction systems with TMB, ABTS and OPD yielded three corresponding absorption peaks at 652, 420 and 450 nm, respectively (Fig. 3a–c), indicating that the enzyme-like activity of the 3D-V_2O_5/NC nanocomposite was not specific to the three chromogenic substrates. Under identical experimental conditions, the absorbance at 450 nm (A_{450}) in the presence of OPD was as low as 0.16 with no obvious color variation. In sharp contrast, the A_{420} value reached as high as 2.58 in the presence of ABTS. Compared to the chromogenic substrates OPD and ABTS, TMB gave the more appropriate absorbance value (1.33) at 652 nm. As for OPD, it not only provided the lower A_{450} value (0.16), but also had strong carcinogenicity compared to TMB. Although the color development reaction of TMB resulted from the similar redox reaction as OPD, the reaction of the former was reversible. If there was a reducing agent, such as vitamin C, in the solution, the color development could quickly subside. With regard to ABTS, its A_{420} value reached as high as 2.58. When the absorbance value was greater than 2.0, the saturated optical density led to a significant decrease in color recognition sensitivity, which would result in a large experimental error due to inaccurate absorbance data. Moreover, the price of ABTS with purity >99.0% is much higher than that of TMB. Based on the above considerations, we selected TMB as the appropriately chromogenic substrate.

3.2.2. Enzymatic activity of 3D-V_2O_5/NC

The 3D-V_2O_5/NC nanocomposite had a large specific surface area, multiple active sites, and an abundance of structural vacancies, which led us to rigorously explore its enzyme-mimetic activity and its underlying catalytic mechanisms. When the solution contained only TMB or 3D-V_2O_5/NC-H_2O_2, the solution was colorless with no corresponding UV–vis absorption (Fig. 3d). The TMB + H_2O_2 system exhibited a weak absorption (A_{652} of 0.17), which possibly originated from the decomposition of some H_2O_2 molecules. When the reaction system included 3D-V_2O_5/NC and TMB, the solution turned light blue and produced a weak absorption peak at 652 nm, suggesting that the 3D-V_2O_5/NC may have a weak OXD-like activity. Only when 3D-V_2O_5/NC, TMB and H_2O_2 were present simultaneously, the solution turned bright blue with pronounced A_{652} values. According to the report by Jing and colleagues, CAT could catalyze H_2O_2 to produce O_2, while POD could decompose H_2O_2 into ·OH [36]. Based on the as-described phenomena and the previous literature, we infer that the 3D-V_2O_5/NC nanocomposite possesses POD-like and/or CAT-like activities along with OXD-like property.

To demonstrate whether the prepared nanocomposites have OXD-like activity and whether O_2 plays a role in the reaction, solution color changes were observed in the presence of 3D-V_2O_5/NC and in the absence of H_2O_2 under an O_2 (oxic) or N_2 (anoxic) atmosphere. A bright

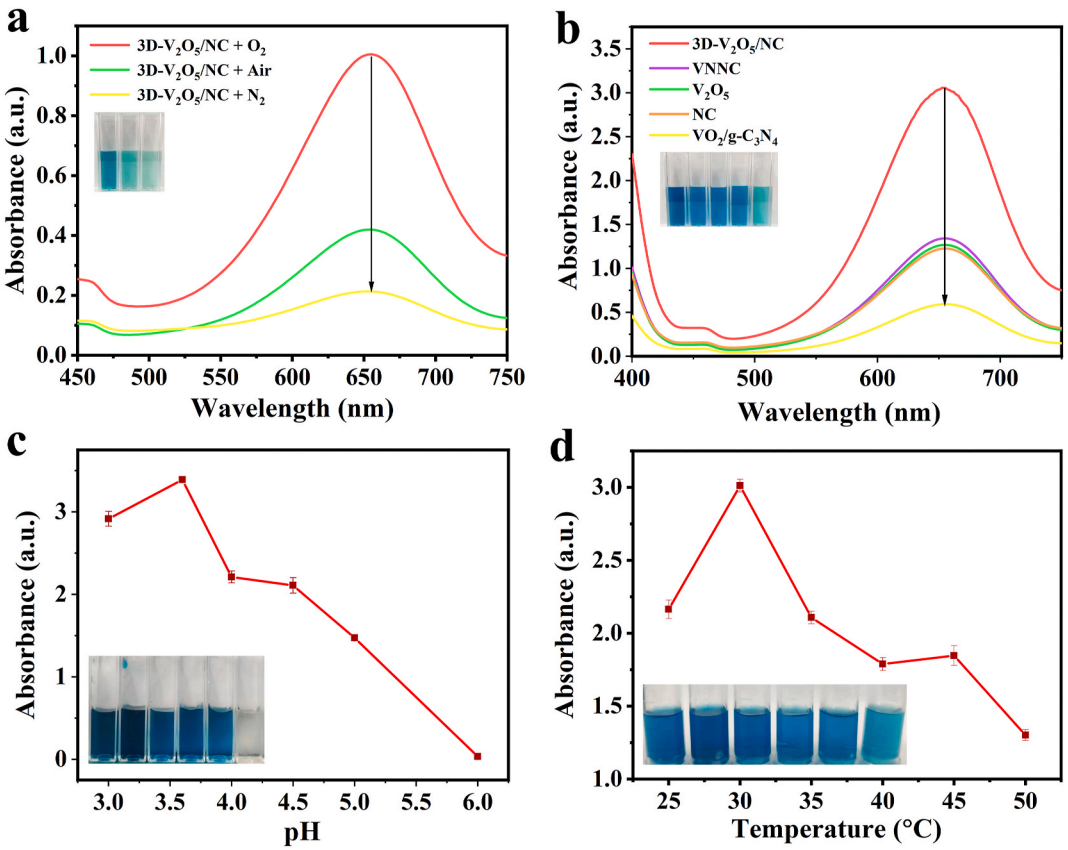

Fig. 4. (a) The UV–vis spectra of the TMB+3D-V_2O_5/NC system in air, O_2 and N_2. (b) Catalytic activities of five nanomaterials (NC, V_2O_5, VN/NC, VO_2/g-C_3N_4, 3D-V_2O_5/NC) on TMB. Effects of (c) pH and (d) temperature on the enzymatic activity of 3D-V_2O_5/NC.

blue color was observed in the presence of O_2, whereas only a weak blue color developed in the N_2 atmosphere (Fig. 4a). To demonstrate whether or not the as-prepared nanocomposite possessed CAT-like activity and H_2O_2 played a crucial role in the reactive system, the following experiments were conducted. Firstly, 250 μg mL^{-1} of 3D-V_2O_5/NC and 50 mM H_2O_2 were added to NaAc-HAc buffer solution (20 mM, pH = 3.6) and incubated for 6 min. Then, the 240-nm absorbance values were recorded using a UV–vis spectrophotometer. As shown in Fig. S7, when the 3D-V_2O_5/NC and H_2O_2 co-existed, the A240 values were significantly reduced, which implied that H_2O_2 was decomposed to a large extent. Building upon the above analyses, it can be concluded that the 3D-V_2O_5/NC nanocomposite might possess both OXD-like and CAT-like activities. More importantly, the CAT-mimetic activity of 3D-V_2O_5/NC is related to the reduction of H_2O_2. To sum up, these phenomena provide compelling evidence that H_2O_2 plays an important role in the chromogenic system. As a result. we selected the 3D-V_2O_5/NC + TMB + H_2O_2 system for further exploration.

3.2.3. Comparison of enzyme activity of 3D-V_2O_5/NC with components and intermediates

To investigate the effect of each component in the nanocomposite on chromogenesis, three experiments were conducted to compare the differential enzyme-like activities for the contrasting nanomaterials (3D-V_2O_5/NC, NC, and V_2O_5). The 3D-V_2O_5/NC + TMB + H_2O_2 system showed the strongest 652-nm absorbance (A_{652} = 3.1), followed by the V_2O_5+TMB + H_2O_2 system (A_{652} = 1.25), and the NC + TMB + H_2O_2 system (A_{652} = 1.2) (Fig. 4b). Obviously, the 3D-V_2O_5/NC nanocomposite with the strongest catalytic capacity might be explained by the fact that the 3D porous nitrogen-doped carbon framework and the ultrafine structure of V_2O_5 nanoparticles effectively improve the number of active sites. Further, the homogeneous anchoring of V_2O_5 nanoparticles onto the carbon substrate facilitates electron transfer in the catalytic reaction, thereby enhancing interactions between the nanozyme and chromogenic substrate. Thus, we posit that compared to its precursors, the enhanced enzyme-like activity of 3D-V_2O_5/NC resulted from synergistic effects between NC and V_2O_5. In addition, the intermediates VN/NC and VO_2/g-C_3N_4 in the material synthesis process were selected for comparative enzymatic activity experiments. Both the VN/NC + TMB + H_2O_2 system (A_{652} = 1.3) and the VO_2/g-C_3N_4+TMB + H_2O_2 system(A_{652} = 0.5) showed much lower absorbance than the 3D-V_2O_5/NC system (Fig. 4b).

3.2.4. Optimization of the important experimental conditions

Across the pH range of 3.2–6.0, the highest A_{652} value was observed at the solution pH 3.6 (Fig. 4c). Further increases or decreases in the pH of the reaction system would lead to the decreasing catalytic activity. Especially, when the pH was close to 6.0, the 3D-V_2O_5/NC almost lost its catalytic activity, indicating that the reaction system is more active in the weakly acidic solutions, which was consistent with previous report [37]. This pH-dependent activity was similar for V_2O_5 and NC nanomaterials (Figs. S8a and d). The acid-enhanced catalytic reactivity of TMB resulted from its limited solubility in aqueous solution, which was improved due to the protonation of one amino group under weak acid conditions [38]. However, the excessive lower solution pH caused the protonation of two amino groups in the TMB molecules, which led to the substrate insusceptibility to catalytic oxidation and further decrease the enzyme-like activity. Similar to natural enzymes, too high or low temperature values significantly inhibit the catalytic effect. For example, A_{652} values gradually increased from 2.12 to 3.02 as the temperature increased from 25 to 30 °C; however, as the temperature further increased from 30 to 50 °C, the 652-nm absorbance decreased dramatically to 1.25. The high temperature possibly affected the nanosheet stability resulting in the lower catalytic capacity.

Increasing the 3D-V_2O_5/NC concentration from 0 to 1 mg/mL resulted in a monotonic increase in the A_{652} value from 0.51 to 3.52 (Fig. S9b). However, as the 3D-V_2O_5/NC concentration exceeded 0.7 mg/mL, there was no further increase in 652-nm absorption. This suggests that the catalytic activity of this nanozyme reached a plateau, and due to substrate limitation, an excessive amount of nanoenzyme did not contribute to further color development [39]. Notably, when A_{652} values exceed 2.0, absorption saturation leads to a decrease in color recognition sensitivity. Moreover, with increasing incubation time from 0 to 30 min, the 652-nm absorbance prominently increased from 0.21 to 1.18 a.u. within 20 min, whereas it remained nearly unchanged (~1.20 a.u.) from 20 to 30 min (Fig. S9a). Synthesizing these experimental results, we ascertained the optimized experimental conditions as follows: incubation temperature, 30 °C; initial solution pH, 3.6; 3D-V_2O_5/NC concentration, 0.25 mg/mL; and incubation time, 20 min.

3.3. Steady-state kinetics of the 3D-V_2O_5/NC nanoenzyme

We next investigated the steady-state kinetics of 3D-V_2O_5/NC nanocomposites under optimized conditions across variable TMB (0.01–0.1 mM) and H_2O_2 (0.01–0.8 mM) concentrations. The Michaelis-Menten constant (K_m) and maximum rate (V_{max}) were calculated based on Lineweaver-Burk plots (Fig. 5a–d). The K_m value for the 3D-V_2O_5/NC-TMB-H_2O_2 mixed system was 0.13 for TMB and 0.12 for H_2O_2. These values were much lower than those for HRP, V_2O_5 and selected vanadium-based nanoenzymes (Table 1), thereby confirming the greater affinity of 3D-V_2O_5/NC for the substrate [40–45]. This nanozyme has better catalytic activity than common HRP, which may be attributable to the multiple active sites on the surface of 3D-V_2O_5/NC nanoparticles.

3.4. Mechanisms associated with the catalytic activity of 3D-V_2O_5/NC

The individual chromotest yielded a preliminary assessment of the enzyme-mimetic activity of 3D-V_2O_5/NC. To elucidate the underlying mechanisms responsible for the catalytic performance of 3D-V_2O_5/NC, a series of ROS capture experiments were conducted using selective scavengers: EDTA for h^+, IPA for ·OH, NaN_3 for $^1O_2$ and PBQ for $\cdot O_2^-$. If the free radical species for catalyzing the reaction was captured by the scavenger, the corresponding response signal would prominently decline. Addition of PBQ scavenger resulted in a significant drop (>96.0%) in the relative activity of 3D-V_2O_5/NC (Fig. 6a), highlighting the crucial role that $\cdot O_2^-$ plays in the catalytic reaction. After the addition of EDTA, the relative activity decreased by ~34.4% as compared to the control without fortification, implying the participation of some h^+ in the catalytic reaction. In contrast, the presence of IPA had no significant effect on the A_{652} value indicating that ·OH has a negligible effect on the catalytic process. That is to say, the synthesized nanocomposite does not have POD-like activity. Owing to the fact that CAT decomposed H_2O_2 to produce O_2, we preliminarily inferred that 3D-V_2O_5/NC has dual enzyme-mimetic activities (i.e., CAT and OXD) and ·OH does not play an important role in the catalytic reactions.

The presence of free radical participation in the 3D-V_2O_5/NC-based catalytic system was further inferred by EPR analysis. As elaborated in Fig. 6b-d and S10, strong characteristic signals for h^+, $^1O_2$, and $\cdot O_2^-$ were detected, with a small ·OH signal due to the presence of H_2O_2. These results indicate that the 3D-V_2O_5/NC nanozyme was able to catalyze H_2O_2 to produce O_2, and further oxidize O_2 to $\cdot O_2^-$ and $^1O_2$ due to its OXD-like activity (Scheme 2). This leads us to conclude that the 3D-V_2O_5/NC nanozyme possesses both CAT-like and OXD-like dual enzymatic activity. The multivalent state of vanadium in the synthesized nanocomposite and the synergistic interactions between vanadium and N-doped carbon accelerate electron transfer and enhance redox capacity, thereby facilitating the catalytic process.

3.5. Colorimetric detection of H_2O_2 and AA

3.5.1. H_2O_2 detection

Based on the 3D-V_2O_5/NC nanozyme, a simple method was developed as a sensing platform for quantitative detection of H_2O_2. In the

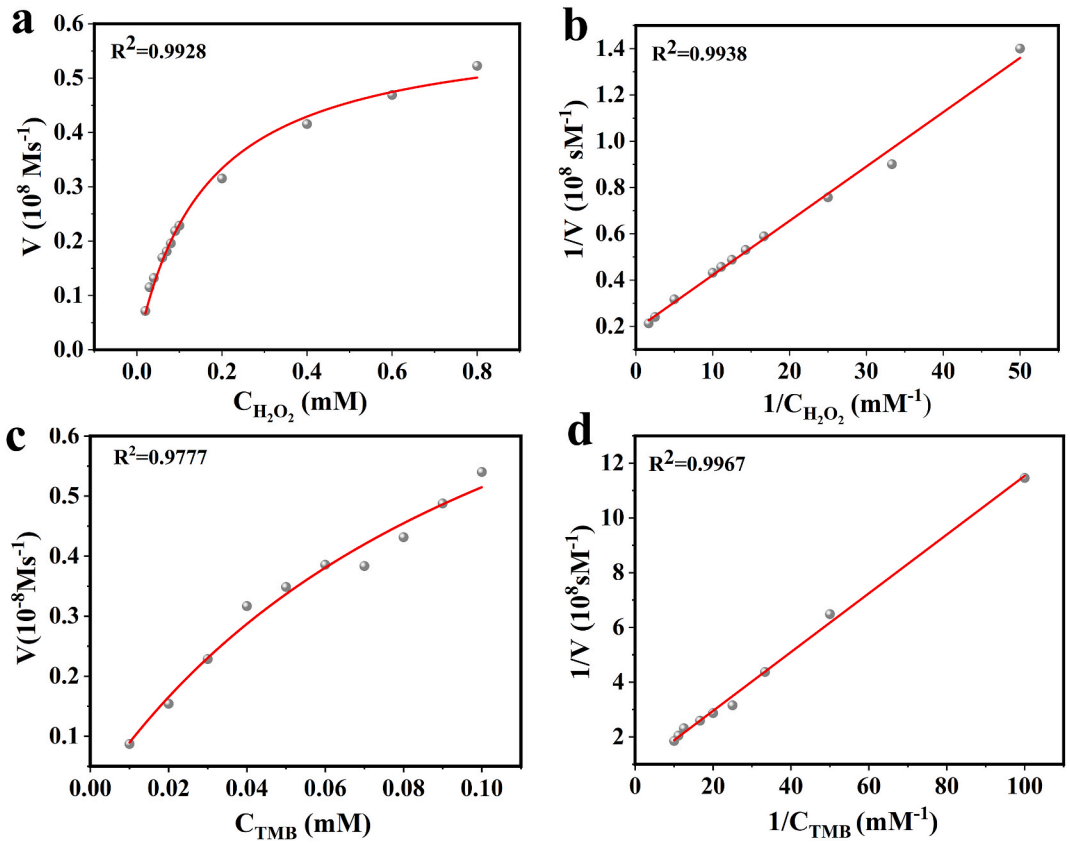

Fig. 5. Michaelis-Menten plots of 3D-V_2O_5/NC fitted for varying (a) H_2O_2 and (c)TMB concentrations; and the associated Lineweaver-Burk plots for (b) H_2O_2 and (d)TMB.

Table 1
Michaelis-Menten constants for H_2O_2 and TMB substrates and their comparison to HRP and other selected nanozymes.

Catalyst	K_m (mM)		V_{max} (10^{-8} M/s)		Refs.
	H_2O_2	TMB	H_2O_2	TMB	
HRP	0.21	2.46	2.46	1.24	[40]
N-doped carbon	0.28	95.8	2.44	410	This work
V_2O_5	0.96	3.30	8.36	3.11	This work
Fe_3O_4 MNPs	154	0.10	9.78	3.34	[41]
VO_2(B)	1.69	0.15	177	131	[42]
VO_2(A)	0.06	0.17	1.40	2.40	[43]
$CeVO_4$	0.16	0.33	8.53	3.61	[44]
V_6O_{13}	7.27	0.15	20.9	15.3	[45]
3D-V_2O_5/NC	0.12	0.13	5.16	12.4	This work

H_2O_2 concentration range of 0–5 mM, the 652-nm absorbance in the mixed system increased monotonically (Fig. 7a). A strong linear relationship was achieved with coefficients of determination (R^2) >0.9961 in the range of 10 μM-1.0 mM and 1.0–5.0 mM (inset of Fig. 7b). The corresponding limit of detection (LOD) was 3.0 μM based on a 3-fold ratio of signal to noise (S/N = 3). As summarized in Table S2, this 3D-V_2O_5/NC-based colorimetric sensor has a high sensitivity for H_2O_2 detection compared to previously reported nanozymes having an absence of 2D carbon nanosheets, such as MOF-818, CoS, V_2O_5–Mt, N-G-Fe_3O_4, CQDs, and V_2O_5–TiO_2 [46–51]. This phenomenon can be explained by the fact that the large specific surface area of 2D carbon nanosheets in the 3D-V_2O_5/NC nanocomposite effectively hinders the agglomeration of V_2O_5 and increases the active sites of the nanozyme. Moreover, owing to the mesoporous structure of carbon nanosheets, 3D-V_2O_5/NC accelerates the electron transfer rate and enhances the interactions between the nanozyme and substrate. These advantageous properties of 3D-V_2O_5/NC enhance the overall sensitivity and improve the analytical performance for H_2O_2 quantification.

3.5.2. AA detection

Antioxidants inhibit oxidative reactions, to some extent, by virtue of their OXD activities. Herein, a typical and common antioxidant AA was chosen as a representative antioxidant for TAC assessment because of its ability to react with and consume free radicals. Several colorimetric tests were performed on varying AA concentrations under optimized experimental conditions as discuss above. Due to its dual enzyme-mimetic activity, the 3D-V_2O_5/NC promoted the oxidation of colorless TMB to a blue TMB_{ox} form. The 652-nm absorbance intensities decreased with increasing AA concentrations from 0 to 500 μM (Fig. 7c). When the dissolved oxygen approached the 3D-V_2O_5/NC nanocomposite, electrons were transferred from the surface to oxygen molecules to produce $^1O_2$ and $\cdot O_2^-$. The addition of AA was conducive to the concentration-dependent reduction of oxTMB, thereby decreasing the 652-nm absorption.

Two concentration-dependent linear relationships were constructed between the 652-nm absorbance change (ΔA) and AA concentration: 0.1–7.0 μM, ΔA = 0.05029[AA] + 0.00499 (R^2 = 0.9980) and 10–500 μM, ΔA = 0.00153[AA] + 0.34799 (R^2 = 0.9963) (Fig. 7d) [14]. Based on a S/N of 3, the LOD for this colorimetric sensor was 0.03 μM. As summarized in Table 2, the constructed sensing platform for the AA assay possesses a wider linear range and lower LOD than previously reported nanozymes [14,52–54], as well as several other electrochemical and chemiluminescent approaches [55–59].

3.6. Interference effects on the constructed sensing platform

To evaluate the selectivity and potential interference effects on this colorimetric method, several interfering substances were fortified into

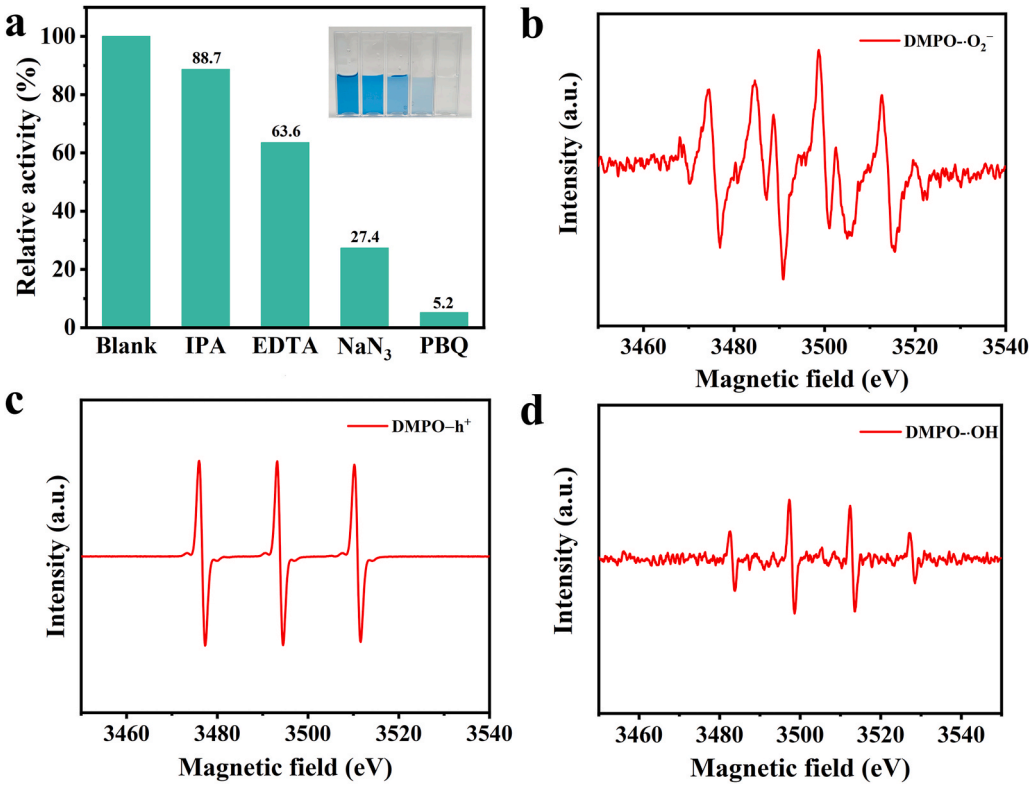

Fig. 6. (a) Effects of active scavengers on the catalysis of TMB in the presence of 3D-V_2O_5/NC; (b, c and d) EPR spectra of 3D-V_2O_5/NC.

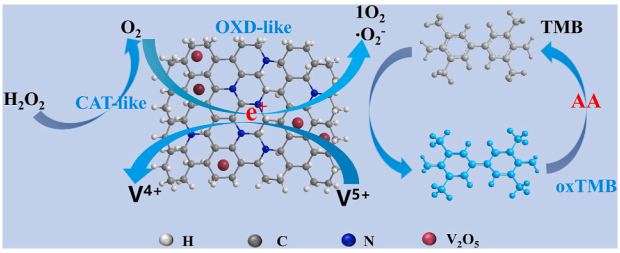

Scheme 2. Proposed mechanism for CAT-like and OXD-like activity of 3D-V_2O_5/NC.

the 3D-V_2O_5/NC-TMB-H_2O_2 reaction system, including metal ions (Na^+, K^+, Ca^{2+}, Mg^{2+}), amino acids (His, Ser, Gly, Try, L-Cys, and Tyr), saccharide (Fru, Suc, Gal, Glu), GSH, CA, H_2Mi and UA. The effects of the aforementioned interfering substances on the AA assay were minimal, except for the antioxidants of L-Cys, UA and GSH (Fig. 8). At the same fortification level as AA, the Cys, UA and GSH biomolecules had lower inhibitory effects than AA, which might be related to their weaker reduction characteristics. These findings suggest that the interference effect from macromolecules and metal ions are in general very low, even at high fortification levels. Thus, we posit that the newly developed sensing platform, based on the 3D-V_2O_5/NC nanozyme, has high selectivity and low interference effects as a AA assay.

3.7. Reproducibility, storage stability and recyclability of the 3D-V_2O_5/NC nanozyme

Upon addition of 0.3 mM AA, the 652-nm absorbance intensity did not differ significantly for five independent batches of 3D-V_2O_5/NC nanocomposite (Fig. 9a), and thus the nanozyme displayed good reproducibility. Similarly, the relatively catalytic activity of 3D-V_2O_5/NC remained >90% after 5 weeks of storage at room-temperature in a sealed container confirming that the nanocomposite had a high storage stability. The reusability of the 3D-V_2O_5/NC nanoenzyme was evaluated by detecting its catalytic activity in reducing blue oxTMB to colorless TMB in the presence of 0.3 mM AA for five consecutive reaction cycles. The enzyme-like activity of 3D-V_2O_5/NC remained greater than 87% after five cycles, highlighting its excellent potential for reuse (Fig. 9c).

3.8. AA assay for vitamin C tablets and TAC assessment for real-world beverage

To validate the reliability and precision of the newly developed method in real-world samples, we determined the AA contents of six commercial vitamin C tablets (the three brands of bioflavonoid-vitamin tablets, multivitamin tablets and two simple vitamin tablets). As shown in Fig. 10a, the detected AA contents for the vitamin C tablets were in general agreement with the specified AA values (25–1000 mg for each tablet), which substantiated the accuracy and reliability of the 3D-V_2O_5/NC based colorimetric method. Further, we estimated the TAC content of six commercial beverages (two juices, one lemon beverage, and three tea samples) based on the linear equation for AA detection. TAC was evaluated in the range of 3.89–21.16 mM with RSDs ≦3.4% in the unfortified samples (Table 3). The reliability of TAC assessment in real drinks was confirmed by adding the real samples with AA at known concentrations. At the two fortification levels (5 and 10 mM), the 3D-V_2O_5/NC-H_2O_2-TMB catalytic system provided relative AA recoveries from 93.0% to 109.5% with RSDs <5.70%.

The analytical performance of the newly developed method was compared with commercial ABTS test kits, in which the absorbance of $ABTS^{\bullet+}$ was measured and used to calculate the TAC content. Trolox is a vitamin E analogue with a similar antioxidant capacity to vitamin E and is commonly used as a TAC reference for other antioxidants. A calibration plot was constructed between the 734-nm absorbance and Trolox concentration generating an R^2 of 0.9777 (Fig. 10b). TAC was detected in the range of 4.24–21.91 mM by the commercial ABTS kits with RSDs ≦3.9% (Table 4). Thus, the 3D-V_2O_5/NC based colorimetric method

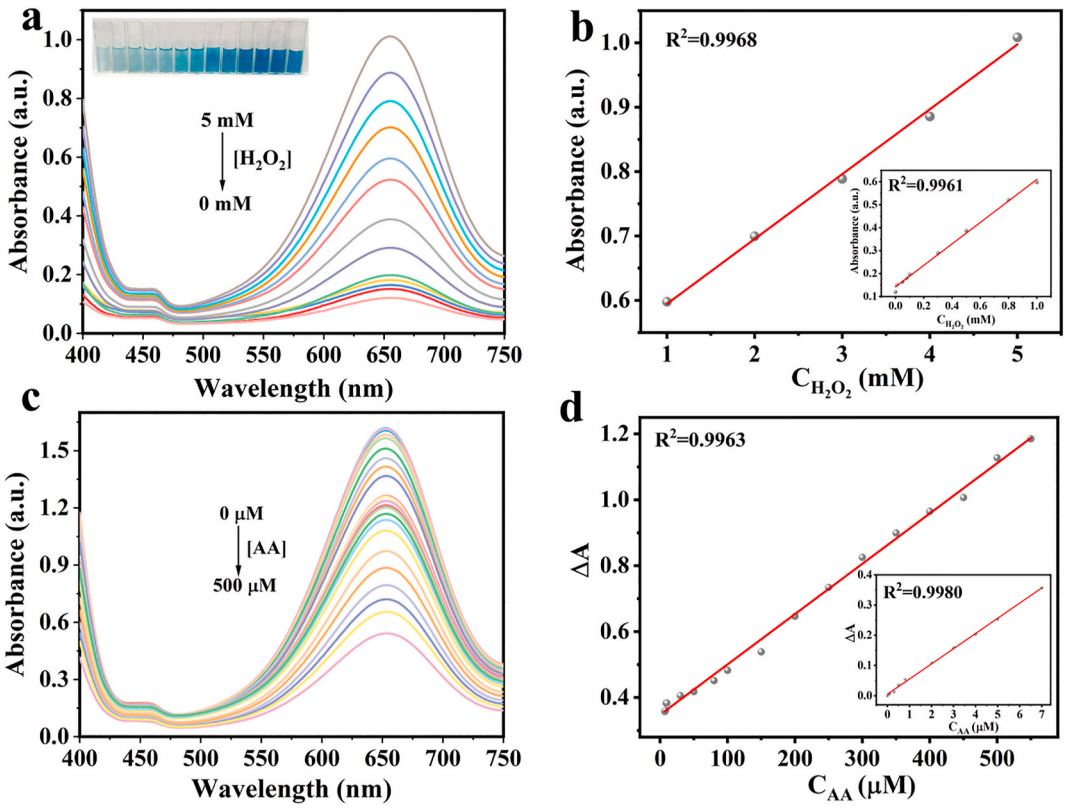

Fig. 7. (a) UV–vis absorbance spectra of TMB/H_2O_2/3D-V_2O_5/NC system in the presence of 0–5 mM H_2O_2. (b) Linear plots of absorbance *vs.* H_2O_2 concentration; Inset shows plot for the 20 μM to 1 mM concentration range. (c) UV–vis absorbance spectra of TMB/H_2O_2/3D-V_2O_5/NC system in the presence of 0–500 μM AA. (d) Linear plots of ΔA *vs.* AA concentration; Inset shows plots for the 0.1–7 μM concentration range. ΔA represents the A_{652} difference before and after addition of AA to the TMB/H_2O_2/3D-V_2O_5/NC system.

Table 2
Comparison of nanomaterial-based methods for determination of AA.

Material	Method	Linear range (μM)	Detection limit (μM)	Refs.
Cu–N–C-700	Colorimetry	0.1–500	0.09	[14]
Fe-NC NTs	Colorimetry	0.2–20	0.13	[52]
SNC-900	Colorimetry	100–5000	80	[53]
N-doped carbon	Colorimetry	0.8–80	35	[54]
CMC-SQDs	Fluorescence	1–300	0.18	[55]
BSA-AuNCs	Fluorescence	3–50	0.40	[56]
Carbon dots	Fluorescence	10–70	3.26	[57]
CBNB/CNTs/GCE	Electrochemistry	20–400	5.71	[58]
NH_2-CQDs	Electrochemistry	0–1000	2.70	[59]
3D-V_2O_5/NC	Colorimetry	0.1–500	0.03	This work

provides similar accuracy and reproducibility to the commercial ABTS kits, thereby documenting its potential for applications requiring TAC monitoring in pharmaceutical and food matrices.

3.9. TAC assessment using a smartphone-based platform

Based on the successful development of the 3D-V_2O_5/NC + TMB + H_2O_2 catalytic system, a smartphone-based colorimetric application (APP) was developed by employing "Thing Identify" software to quantify TAC (Fig. 11a). The overall operational procedures and detailed description for the APP are shown in Fig. S1. As exhibited on the smartphone screen of Fig. 11b, the color intensities monotonically decreases with increasing AA concentrations. Thus, a calibration curve was generated by plotting the color grayscale values for the reaction solution

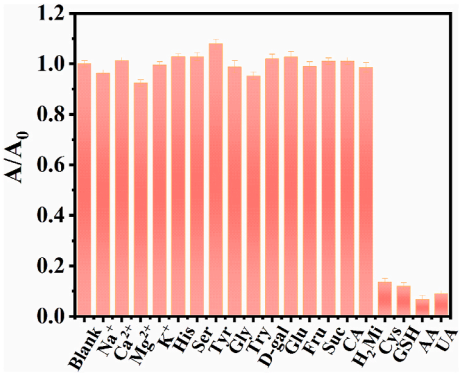

Fig. 8. Effects of potentially interfering substances on A_{652} of the TMB/H_2O_2/3D-V_2O_5/NC system relative to the non-fortified blank (mean ± SD). Experimental conditions: 10 mM of Na^+, Ca^{2+}, Mg^{2+}, K^+, His, Ser, Gly, Try, Tyr, Fru, Suc, Gal, Glu, CA, and H_2Mi; 1 mM of UA, AA, L-Cys, and GSH.

against the corresponding AA concentrations. A strong linear relationship was acquired across the AA concentration range of 1–500 μM with a regression equation of Y = 11.369 × X-861.89 (R^2 = 0.971), where X and Y are color grayscale value and the AA concentration, respectively. The LOD was 0.3 μM based on a S/N of 3, and the AA concentrations detected by the APP were comparable to the test results using conventional TAC assay kits (Table 4). In sum, the newly developed smartphone-based colorimetric platform possesses several prominent advantageous, such as simple, rapid and low-cost operation, portability, high throughput, feasibility for outdoor use, and adaptability for point-of-care applications.

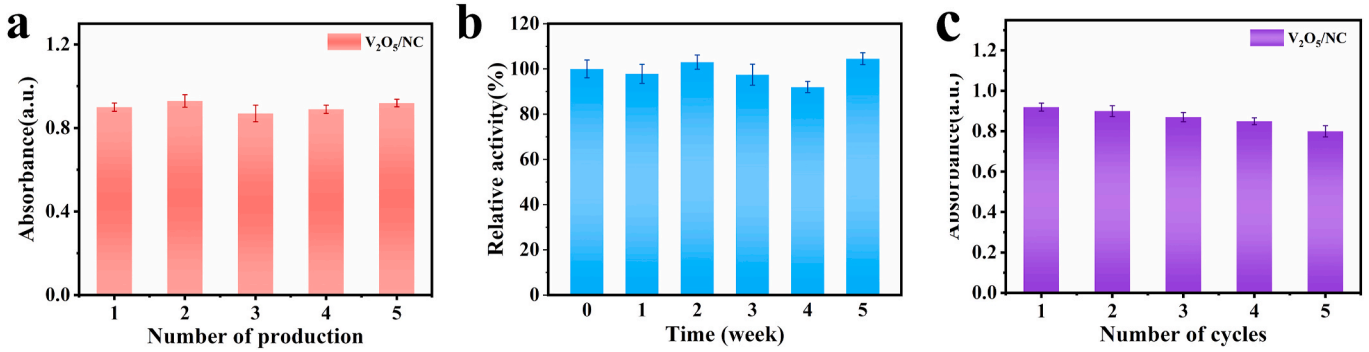

Fig. 9. (a) Repeatability, (b) storage stability, and (c) reuse cycle effects on AA detection by the synthesized V_2O_5/NC colorimetric sensor (mean ± SD).

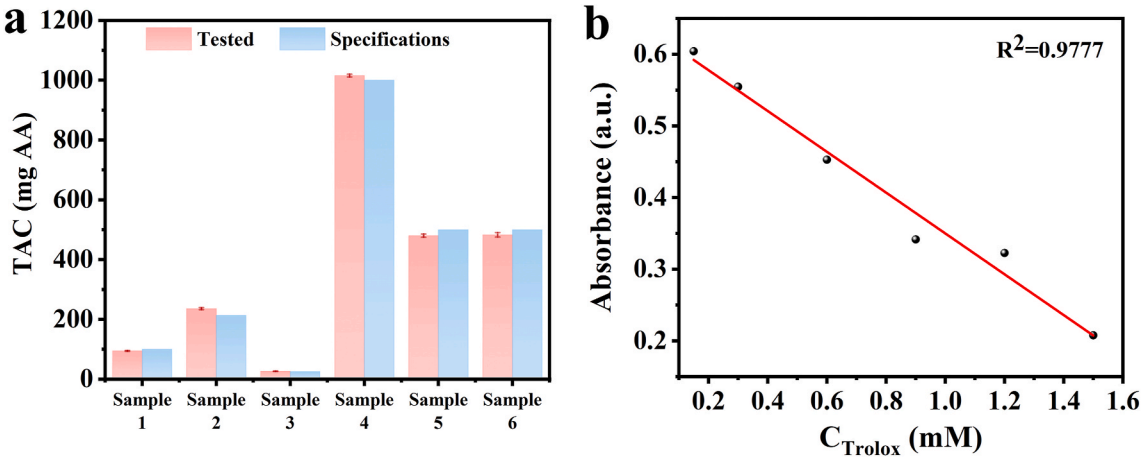

Fig. 10. (a) TAC of six commercial vitamin C tablets (mean ± SD), and (b) standard curve for Trolox using a commercial ABTS test kit.

Table 3
TAC assessment for six commercial beverages and AA recovery in the corresponding drinks.

Samples	TAC (mM)	RSD% (n = 3)	AA added (mM)	Equivalent AA found (mM)	AA recovery (%)	RSD% (n = 3)
Orange juice	7.60	0.8	5	11.72	93.0	5.7
			10	18.03	102.4	3.0
Grape juice	7.51	3.4	5	12.55	100.3	2.7
			10	18.03	103.0	5.3
Lemon beverage	7.01	2.8	5	13.22	101.6	3.0
			10	18.01	105.9	4.2
Pu'er tea	3.89	2.7	5	9.36	105.3	3.0
			10	15.21	109.5	1.3
Oolong tea	21.16	2.9	5	27.68	105.8	2.2
			10	32.17	103.2	5.4
Black tea	5.41	2.9	5	10.32	99.1	2.3
			10	15.67	101.7	5.1

Table 4
TAC assessment by three methods in six commercial beverages.

Samples	TMB assay (mM)	RSD% (n = 3)	TAC assay kit (mM)	RSD% (n = 3)	Smartphone-based assay (mM)	RSD% (n = 3)
Orange juice	7.60	0.8	7.50	3.2	7.52	1.8
Graper juice	7.51	3.4	7.70	2.7	7.55	2.4
Lemon beverage	7.01	2.8	7.04	3.9	7.18	3.0
Pu'er tea	3.89	2.7	4.24	2.6	3.95	3.2
Oolong tea	21.16	2.9	21.91	2.3	21.24	1.5
Black tea	5.41	2.9	5.29	2.5	5.39	3.6

4. Conclusions

Total antioxidant capacity (TAC) is an important parameter for evaluating the quality of antioxidant foods and monitoring the level of oxidative stress in humans. Herein, a 3D-V_2O_5/NC nanocomposite with OXD-like and CAT-like activities was successfully fabricated using a self-templating method. The synthesized nanocomposite had strong catalytic properties due to the generation of three free radicals ($^1O_2$, h^+, $\cdot O_2^-$) and

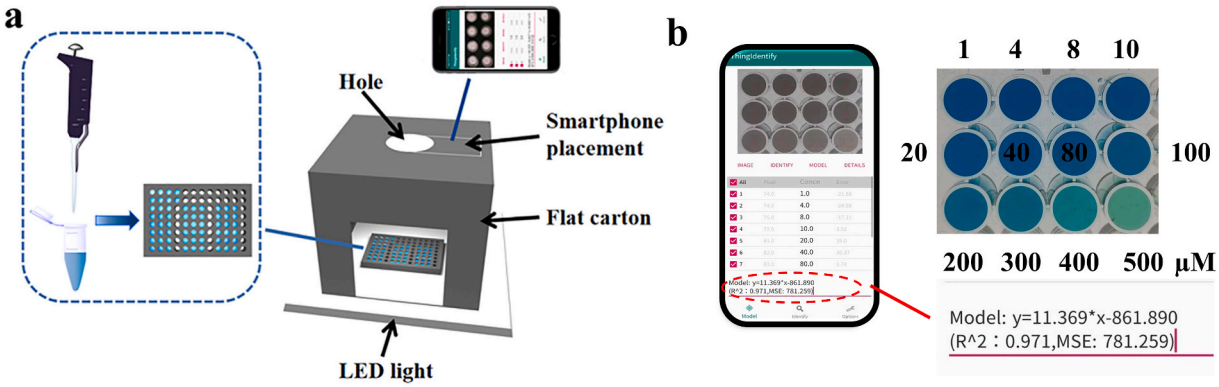

Fig. 11. (a) Schematic of smartphone-based platform for TAC quantification; and (b) Regression equation between absorbance and TAC concentrations (1–500 μM).

the synergistic effect between N-doped carbon lamellae and V_2O_5 nanoparticles that coexisted in multivalent states. Based on the dual enzyme-like activities of 3D-V_2O_5/NC, a highly selective/sensitive sensor was constructed for TAC assessment. The newly developed colorimetric platform had a detection limit of 0.03 μM for AA and relative recovery of 93.0–109.5% for AA, which were comparable with commercial ABTS test kits. The newly developed sensor was successfully deployed in a smartphone-based detection platform based on "Thing Identify" software. The method was successfully tested for *in-situ* TAC assessment of vitamin C tablets and a range of beverages, thereby demonstrating strong feasibility for remote outdoor or point-of-care applications.

CRediT authorship contribution statement

Qi Wang: Formal analysis, Investigation, Methodology, Data curation, Writing – original draft. **Yongli Ding:** Formal analysis, Investigation, Resources, Writing – original draft. **Randy A. Dahlgren:** Formal analysis, Writing – review & editing. **Yue Sun:** Methodology, Validation. **Jingjing Gu:** Investigation, Resources. **Yuhao Li:** Data curation, Formal analysis. **Tingting Liu:** Validation, Formal analysis, Supervision, Writing – review & editing. **Xuedong Wang:** Conceptualization, Funding acquisition, Supervision, Writing – review & editing.

Declaration of competing interest

The authors declare that they have no known competing financial interests or personal relationships that could have appeared to influence the work reported in this paper.

Data availability

The authors do not have permission to share data.

Acknowledgement

This work was jointly supported by the National Science Foundation of China (22076134), Jiangsu Provincial Natural Science Foundation (BK20211338), Key Science & Technology Project of Suzhou City (SS202028), and Jiangsu Provincial Key Research & Development Program (BE2022733).

Appendix A. Supplementary data

Supplementary data to this article can be found online at https://doi.org/10.1016/j.aca.2023.341072.

References

[1] Y. Shi, Z. Liu, R. Liu, R. Wu, J. Zhang, DNA-encoded MXene-Pt nanozyme for enhanced colorimetric sensing of mercury ions, Chem Eng J 442 (2022), 136072, https://doi.org/10.1016/j.cej.2022.136072.
[2] M.A. Wahab, S.M.A. Hossain, M.K. Masud, H. Park, A. Ashok, M. Mustapić, M. Kim, D. Patel, M. Shahbazi, M.S.A. Hossain, Y. Yamauchi, Y.V. Kaneti, Nanoarchitectured superparamagnetic iron oxide-doped mesoporous carbon nanozymes for glucose sensing, Sens. Actuators, B 366 (2022), 131980, https://doi.org/10.1016/j.snb.2022.131980.
[3] R. Li, X. He, R. Javed, J. Cai, H. Cao, X. Liu, Q. Chen, D. Ye, H. Zhao, Switching on-off-on colorimetric sensor based on Fe-N/S-C single-atom nanozyme for ultrasensitive and multimodal detection of Hg^{2+}, Sci. Total Environ. 834 (2022), 155428 https://doi.org/10.1016/j.scitotenv.2022.155428.
[4] Y. Chen, W. Nie, Z. Peng, F. Yu, J. Yang, Y. Li, Strontium oxides with enzyme-like activity: a colorimetric sensor array for highly sensitive discrimination of bisphenols, Sens. Actuators, B 364 (2022), 131869, https://doi.org/10.1016/j.snb.2022.131869.
[5] X. Zhang, G. Han, R. Zhang, Z. Huang, H. Shen, P. Su, J. Song, Y. Yang, $Co_2V_2O_7$ particles with intrinsic multienzyme mimetic activities as an effective bioplatform for ultrasensitive fluorometric and colorimetric biosensing, ACS Appl. Bio Mater. 3 (2020) 1469–1480, https://doi.org/10.1021/acsabm.9b01107.
[6] L. Zhang, P. Xie, H. Wu, J. Zhao, S. Wang, 2D $MoSe_2$@PVP nanosheets with multi-enzyme activity alleviate the acute pancreatitis via scavenging the reactive oxygen and nitrogen species, Chem Eng J 446 (2022), 136792, https://doi.org/10.1016/j.cej.2022.136792.
[7] J. Li, T. Liu, R.A. Dahlgren, H. Ye, Q. Wang, Y. Ding, M. Gao, X. Wang, H. Wang, N, S-co-doped carbon/$Co_{1-x}S$ nanocomposite with dual-enzyme activities for a smartphone-based colorimetric assay of total cholesterol in human serum, Anal. Chim. Acta 1204 (2022), 339703, https://doi.org/10.1016/j.aca.2022.339703.
[8] F. Natalio, R. André, S.A. Pihan, M. Humanes, R. Wever, W. Tremel, V_2O_5 nanowires with an intrinsic iodination activity leading to the formation of self-assembled melanin-like biopolymers, J. Mater. Chem. 21 (2011), 11923, https://doi.org/10.1039/c1jm11811k.
[9] A. Zeb, X. Xie, A.B. Yousaf, M. Imran, T. Wen, Z. Wang, H.L. Guo, Y.F. Jiang, I. A. Qazi, A.W. Xu, Highly efficient fenton and enzyme-mimetic activities of mixed-phase VO_x nanoflakes, ACS Appl. Mater. Interfaces 8 (2016) 30126–30132, https://doi.org/10.1021/acsami.6b09557.
[10] Y. Ding, G. Ren, G. Wang, M. Lu, J. Liu, K. Li, Y. Lin, V_2O_5 nanobelts mimicking tandem enzymes to achieve nonenzymatic online monitoring of glucose in living rat brain, Anal. Chem. 92 (2020) 4583–4591, https://doi.org/10.1021/acs.analchem.9b05872.
[11] D. Zhai, H. Du, B. Li, Y. Zhu, F. Kang, Porous graphitic carbons prepared by combining chemical activation with catalytic graphitization, Carbon 49 (2011) 725–729, https://doi.org/10.1016/j.carbon.2010.09.057.
[12] L. Parashuram, M.K. Prashanth, P. Krishnaiah, C.B.P. Kumar, F.A. Alharti, K. Y. Kumar, B.H. Jeon, M.S. Raghu, Nitrogen doped carbon spheres from tamarindus indica shell decorated with vanadium pentoxide; photoelectrochemical water splitting, photochemical hydrogen evolution & degradation of bisphenol A, Chemosphere 287 (2022), 132348, https://doi.org/10.1016/j.chemosphere.2021.132348.
[13] Y. Hou, Y. Lu, X. Zhang, Y. Huang, MOF-derived N-doped porous carbon with active magnesium sites as an efficient oxidase mimic for biosensing, Sens. Actuators, B 370 (2022), 132409, https://doi.org/10.1016/j.snb.2022.132409.
[14] Y. Hou, Y. Lu, Q. Chen, X. Zhang, Y. Huang, Ultrathin two-dimensional carbon nanosheets with highly active Cu-N_x sites as specific peroxidase mimic for determining total antioxidant capacity, Sens. Actuators, B 333 (2021), 129549, https://doi.org/10.1016/j.snb.2021.129549.
[15] B. Jiang, M. Liang, Advances in single-atom nanozymes research, Chin. J. Chem. 39 (2021) 174–180, https://doi.org/10.1002/cjoc.202000383.
[16] Y. Fan, J. Li, Y. Guo, L. Xie, G. Zhang, Digital image colorimetry on smartphone for chemical analysis: a review, Measurement 171 (2021), 108829, https://doi.org/10.1016/j.measurement.2020.108829.

[17] X. Zhu, J. Tang, X. Ouyang, Y. Liao, H. Feng, J. Yu, L. Chen, Y. Lu, Y. Yi, L. Tang, Multifunctional MnCo@C yolk-shell nanozymes with smartphone platform for rapid colorimetric analysis of total antioxidant capacity and phenolic compounds, Biosens. Bioelectron. 216 (2022), 114652, https://doi.org/10.1016/j.bios.2022.114652.

[18] W. Liu, J. Tian, C. Mao, Z. Wang, J. Liu, R.A. Dahlgren, L. Zhang, X. Wang, Sulfur vacancy promoted peroxidase-like activity of magnetic greigite (Fe_3S_4) for colorimetric detection of serum glucose, Anal. Chim. Acta 1127 (2020) 246–255, https://doi.org/10.1016/j.aca.2020.06.056.

[19] Y. Fu, Z. Zhao, Y. Shi, K. Xu, J. Zhang, H. Niu, Y. Xu, Hybridization chain reaction-mediated Fe_2MoO_4 bimetallic nanozyme for colorimetric risk prediction of bladder cancer, Biosens. Bioelectron. 210 (2022), 114272, https://doi.org/10.1016/j.bios.2022.114272.

[20] C. Song, H. Liu, L. Zhang, J. Wang, C. Zhao, Q. Xu, C. Yao, FeS nanoparticles embedded in 2D carbon nanosheets as novel nanozymes with peroxidase-like activity for colorimetric and fluorescence assay of H_2O_2 and antioxidant capacity, Sens. Actuators, B 353 (2022), 131131, https://doi.org/10.1016/j.snb.2021.131131.

[21] C. Zhao, Y. Chen, C. Li, Q. Zhang, P. Chen, K. Shi, Y. Wu, Y. He, One step and fast preparation of VO_x/g-C_3N_4 photocatalyst via microwave heating for effective degradation of RhB under visible light, J. Phys. Chem. Solid. 136 (2020), 109122, https://doi.org/10.1016/j.jpcs.2019.109122.

[22] H. Yang, P. Ning, H. Cao, M. Yuan, J. Feng, J. Yue, Z. Liu, G. Xu, Y. Li, Selectively anchored vanadate host for self-boosting catalytic synthesis of ultra-fine vanadium nitride/nitrogen-doped hierarchical carbon hybrids as superior electrode materials, Electrochim. Acta 332 (2020), 135387, https://doi.org/10.1016/j.electacta.2019.135387.

[23] D.J. Li, U.N. Maiti, J. Lim, D.S. Choi, W.J. Lee, Y. Oh, G.Y. Lee, S.O. Kim, Molybdenum sulfide/N-doped CNT forest hybrid catalysts for high-performance hydrogen evolution reaction, Nano Lett. 14 (2014) 1228–1233, https://doi.org/10.1021/nl404108a.

[24] X. Kuai, K. Li, J. Chen, H. Wang, J. Yao, C.L. Chiang, T. Liu, H. Ye, J. Zhao, Y.G. Lin, L. Zhang, V. Nicolosi, L. Gao, Interfacial engineered vanadium oxide nanoheterostructures synchronizing high-energy and long-term potassium-ion storage, ACS Nano (2022), https://doi.org/10.1021/acsnano.1c09935.

[25] H. Wang, Q. Lu, Y. Liu, H. Li, Y. Zhang, S. Yao, A dual-signal readout sensor for highly sensitive detection of iodide ions in urine based on catalase-like reaction of iodide ions and N-doped C-dots, Sens. Actuators, B 250 (2017) 429–435, https://doi.org/10.1016/j.snb.2017.04.117.

[26] M. Preeyanghaa, V. Vinesh, B. Neppolian, Construction of S-scheme 1D/2D rod-like g-C_3N_4/V_2O_5 heterostructure with enhanced sonophotocatalytic degradation for Tetracycline antibiotics, Chemosphere 287 (2022), 132380, https://doi.org/10.1016/j.chemosphere.2021.132380.

[27] J. Zhang, J. Fu, K. Dai, Graphitic carbon nitride/antimonene van der Waals heterostructure with enhanced photocatalytic CO_2 reduction activity, J. Mater. Sci. Technol. 116 (2022) 192–198, https://doi.org/10.1016/j.jmst.2021.10.045.

[28] W. Liu, L. Chu, C. Zhang, P. Ni, Y. Jiang, B. Wang, Y. Lu, C. Chen, Hemin-assisted synthesis of peroxidase-like Fe-N-C nanozymes for detection of ascorbic acid-generating bio-enzymes, Chem Eng J 415 (2021), 128876, https://doi.org/10.1016/j.cej.2021.128876.

[29] H. Yu, L. Shang, T. Bian, R. Shi, G.I. Waterhouse, Y. Zhao, C. Zhou, L.Z. Wu, C. H. Tung, T. Zhang, Nitrogen-doped porous carbon nanosheets templated from g-C_3N_4 as metal-free electrocatalysts for efficient oxygen reduction reaction, Adv Mater 28 (2016) 5080–5086, https://doi.org/10.1002/adma.201600398.

[30] P. Xia, B. Zhu, J. Yu, S. Cao, M. Jaroniec, Ultra-thin nanosheet assemblies of graphitic carbon nitride for enhanced photocatalytic CO_2 reduction, J. Mater. Chem. 5 (2017) 3230–3238, https://doi.org/10.1039/c6ta08310b.

[31] Y. Hong, Y. Jiang, C. Li, W. Fan, X. Yan, M. Yan, W. Shi, In-situ synthesis of direct solid-state Z-scheme V_2O_5/g-C_3N_4 heterojunctions with enhanced visible light efficiency in photocatalytic degradation of pollutants, Appl. Catal. B Environ. 180 (2016) 663–673, https://doi.org/10.1016/j.apcatb.2015.06.057.

[32] H. Song, C. Liu, C. Zhang, G. Cao, Self-doped V^{4+}–V_2O_5 nanoflake for 2 Li-ion intercalation with enhanced rate and cycling performance, Nano Energy 22 (2016) 1–10, https://doi.org/10.1016/j.nanoen.2016.02.004.

[33] F. Zheng, Y. Yang, Q. Chen, High lithium anodic performance of highly nitrogen-doped porous carbon prepared from a metal-organic framework, Nat. Commun. 5 (2014) 5261, https://doi.org/10.1038/ncomms6261.

[34] H. Wang, M. Zhang, K. Wei, Y. Zhao, H. Nie, Y. Ma, Y. Zhou, H. Huang, Y. Liu, M. Shao, Z. Kang, Pyrrolic nitrogen dominated the carbon dot mimic oxidase activity, Carbon 179 (2021) 692–700, https://doi.org/10.1016/j.carbon.2021.04.061.

[35] B. Wang, Y. Bian, S. Feng, S.-q. Wang, B.-x. Shen, Modification of the V_2O_5-WO_3/TiO_2 catalyst with Nb to reduce its activity for SO_2 oxidation during the selective catalytic reduction of NO, J. Fuel Chem. Technol. 50 (2022) 503–512, https://doi.org/10.1016/s1872-5813(21)60177-9.

[36] Y. Jing, J. Li, X. Zhang, M. Sun, Q. Lei, B. Li, J. Yang, H. Li, C. Li, X. Yang, L. Xie, Catalase-integrated metal-organic framework with synergetic catalytic activity for colorimetric sensing, Environ. Res. 207 (2022), 112147, https://doi.org/10.1016/j.envres.2021.112147.

[37] F. Honarasa, F.H. Kamshoori, S. Fathi, Z. Motamedifar, Carbon dots on V_2O_5 nanowires are a viable peroxidase mimic for colorimetric determination of hydrogen peroxide and glucose, Mikrochim. Acta 186 (2019) 234, https://doi.org/10.1007/s00604-019-3344-6.

[38] M. Drozd, M. Pietrzak, P.G. Parzuchowski, E. Malinowska, Pitfalls and capabilities of various hydrogen donors in evaluation of peroxidase-like activity of gold nanoparticles, Anal. Bioanal. Chem. 408 (2016) 8505–8513, https://doi.org/10.1007/s00216-016-9976-z.

[39] N. Khaliq, M.A. Rasheed, M. Khan, M. Maqbool, M. Ahmad, S. Karim, A. Nisar, P. Schmuki, S.O. Cho, G. Ali, Voltage-switchable biosensor with gold nanoparticles on TiO_2 nanotubes decorated with CdS quantum dots for the detection of cholesterol and H_2O_2, ACS Appl. Mater. Interfaces 13 (2021) 3653–3668, https://doi.org/10.1021/acsami.0c19979.

[40] F. Qiao, L. Chen, X. Li, L. Li, S. Ai, Peroxidase-like activity of manganese selenide nanoparticles and its analytical application for visual detection of hydrogen peroxide and glucose, Sens. Actuators, B 193 (2014) 255–262, https://doi.org/10.1016/j.snb.2013.11.108.

[41] B. Jiang, D. Duan, L. Gao, M. Zhou, K. Fan, Y. Tang, J. Xi, Y. Bi, Z. Tong, G.F. Gao, N. Xie, A. Tang, G. Nie, M. Liang, X. Yan, Standardized assays for determining the catalytic activity and kinetics of peroxidase-like nanozymes, Nat. Protoc. 13 (2018) 1506–1520, https://doi.org/10.1038/s41596-018-0001-1.

[42] G. Nie, L. Zhang, J. Lei, L. Yang, Z. Zhang, X. Lu, C. Wang, Monocrystalline VO_2 (B) nanobelts: large-scale synthesis, intrinsic peroxidase-like activity and application in biosensing, J. Mater. Chem. 2 (2014) 2910, https://doi.org/10.1039/c3ta15051h.

[43] L. Zhang, F. Xia, Z. Song, N.A.S. Webster, H. Luo, Y. Gao, Synthesis and formation mechanism of VO_2(A) nanoplates with intrinsic peroxidase-like activity, RSC Adv. 5 (2015) 61371–61379, https://doi.org/10.1039/c5ra11014a.

[44] H. Yang, J. Zha, P. Zhang, Y. Qin, T. Chen, F. Ye, Fabrication of $CeVO_4$ as nanozyme for facile colorimetric discrimination of hydroquinone from resorcinol and catechol, Sens. Actuators, B 247 (2017) 469–478, https://doi.org/10.1016/j.snb.2017.03.042.

[45] H. Zeng, Y. Tang, W. Zou, C. Wang, H. Tao, Y. Wu, V_6O_{13} nanobelts for simultaneous detection of Cd(II) and Pb(II) in water, ACS Appl. Nano Mater. 4 (2021) 4654–4664, https://doi.org/10.1021/acsanm.1c00277.

[46] K. Yu, M. Li, H. Chai, Q. Liu, X. Hai, M. Tian, L. Qu, T. Xu, G. Zhang, X. Zhang, MOF-818 nanozyme-based colorimetric and electrochemical dual-mode smartphone sensing platform for in situ detection of H_2O_2 and H_2S released from living cells, Chem Eng J 451 (2023), 138321, https://doi.org/10.1016/j.cej.2022.138321.

[47] H. Yang, J. Zha, P. Zhang, Y. Xiong, L. Su, F. Ye, Sphere-like CoS with nanostructures as peroxidase mimics for colorimetric determination of H_2O_2 and mercury ions, RSC Adv. 6 (2016) 66963–66970, https://doi.org/10.1039/c6ra16619a.

[48] X. Zhu, Y. Xue, S. Han, W. Chen, M. Fu, Y. Gao, S. Nie, Q. Liu, X. Zhang, X. Zhang, V_2O_5-montmorillonite nanocomposites of peroxidase-like activity and their application in the detection of H_2O_2 and glutathione, Appl. Clay Sci. 195 (2020), 105718, https://doi.org/10.1016/j.clay.2020.105718.

[49] W. Zhang, C. Chen, D. Yang, G. Dong, S. Jia, B. Zhao, L. Yan, Q. Yao, A. Sunna, Y. Liu, Optical biosensors based on Nitrogen-doped graphene functionalized with magnetic nanoparticles, Adv. Mater. Interfac. 3 (2016), 1600590, https://doi.org/10.1002/admi.201600590.

[50] D. He, C. Zheng, Q. Wang, C. He, Y.I. Lee, L. Wu, X. Hou, Dielectric barrier discharge-assisted one-pot synthesis of carbon quantum dots as fluorescent probes for selective and sensitive detection of hydrogen peroxide and glucose, Talanta 142 (2015) 51–56, https://doi.org/10.1016/j.talanta.2015.04.033.

[51] D. Manoj, S. Rajendran, F. Gracia, S. Ansar, M. Santhamoorthy, M. Soto-Moscoso, M.A. Gracia-Pinilla, Improving the sensitivity for hydrogen peroxide determination with active V_2O_5 nanocubes incorporated on mesoporous TiO_2, Environ. Res. 215 (2022), 114427, https://doi.org/10.1016/j.envres.2022.114427.

[52] N. Song, M. Zhong, J. Xu, C. Wang, X. Lu, Single-atom iron confined within polypyrrole-derived carbon nanotubes with exceptional peroxidase-like activity for total antioxidant capacity, Sens. Actuators, B 351 (2022), 130969, https://doi.org/10.1016/j.snb.2021.130969.

[53] Y. Chen, L. Jiao, H. Yan, W. Xu, Y. Wu, H. Wang, W. Gu, C. Zhu, Hierarchically porous S/N co-doped carbon nanozymes with enhanced peroxidase-like activity for total antioxidant capacity biosensing, Anal. Chem. 92 (2020) 13518–13524, https://doi.org/10.1021/acs.analchem.0c02982.

[54] Z. Lou, S. Zhao, Q. Wang, H. Wei, N-doped carbon as peroxidase-like nanozymes for total antioxidant capacity assay, Anal. Chem. 91 (2019) 15267–15274, https://doi.org/10.1021/acs.analchem.9b04333.

[55] S. Chandra, V.K. Singh, P.K. Yadav, D. Bano, V. Kumar, V.K. Pandey, M. Talat, S. H. Hasan, Mustard seeds derived fluorescent carbon quantum dots and their peroxidase-like activity for colorimetric detection of H_2O_2 and ascorbic acid in a real sample, Anal. Chim. Acta 1054 (2019) 145–156, https://doi.org/10.1016/j.aca.2018.12.024.

[56] A.K. Baytak, M. Aslanoglu, A novel sensitive method for the simultaneous determination of ascorbic acid, dopamine, uric acid and tryptophan using a voltammetric platform based on carbon black nanoballs, Arab. J. Chem. 13 (2020) 1702–1711, https://doi.org/10.1016/j.arabjc.2018.01.005.

[57] X. Zhou, Q. Qu, L. Wang, L. Li, S. Li, K. Xia, Nitrogen dozen carbon quantum dots as one dual function sensing platform for electrochemical and fluorescent detecting ascorbic acid, J Nanopart Res 22 (2020), https://doi.org/10.1007/s11051-019-4741-9.

[58] Y. Duan, J. Tan, Z. Huang, Q. Deng, S. Liu, G. Wang, L. Li, L. Zhou, Facile synthesis of carboxymethyl cellulose sulfur quantum dots for live cell imaging and sensitive detection of Cr(VI) and ascorbic acid, Carbohydr. Polym. 249 (2020), 116882, https://doi.org/10.1016/j.carbpol.2020.116882.

[59] P. Ni, S. Liu, B. Wang, C. Chen, Y. Jiang, C. Zhang, J. Chen, Y. Lu, Light-responsive Au nanoclusters with oxidase-like activity for fluorescent detection of total antioxidant capacity, J. Hazard Mater. 411 (2021), 125106, https://doi.org/10.1016/j.jhazmat.2021.125106.